International Journal of Plasticity 169 (2023) 103720

Contents lists available at ScienceDirect

International Journal of Plasticity

journal homepage: www.elsevier.com/locate/ijplas

Effect of Si on the evolution of plasticity mechanisms, grain refinement and hardness during high-pressure torsion of a non-equiatomic CoCrMnNi multi-principal element alloy

Kaushal Kishore [a,b,1], Avanish Kumar Chandan [a,c,1,*], Pham Tran Hung [d], Saurabh Kumar [e], Manish Ranjan [f], Megumi Kawasaki [g], Jenő Gubicza [d,**]

[a] *Academy of Scientific and Innovative Research (AcSIR), Ghaziabad 201002, India*
[b] *Research & Development, Tata Steel Limited, Jamshedpur 831007, India*
[c] *Materials Engineering Division, National Metallurgical Laboratory CSIR, Jamshedpur 831007, India*
[d] *Department of Materials Physics, Eötvös Loránd University, P.O.B. 32, Budapest H-1518, Hungary*
[e] *Department of Metallurgical Engineering and Materials Science, Indian Institute of Technology Bombay, Mumbai 400076, India*
[f] *Department of Materials Science and Engineering, Indian Institute of Technology, Kanpur 208016, India*
[g] *School of Mechanical, Industrial and Manufacturing Engineering, Oregon State University, Corvallis, OR 97331, USA*

ARTICLE INFO

Keywords:
Dislocations (A)
Microstructures (A)
Strengthening mechanisms (A)
Twinning (A)
Multi-principal element alloy

ABSTRACT

The present study unraveled the defining role of small silicon (Si) addition (5 atomic %) in dramatically altering the plasticity mechanisms, grain refinement and hardening response of a non-equiatomic CoCrMnNi multi-principal element alloy (MPEA) during high-pressure torsion (HPT) processing. Both the Si-free and the Si-added MPEAs had a face-centered cubic (FCC) structure and were subjected to a quasi-constrained HPT processing at 6 GPa pressure to different number of turns (0.5 and 5). Microstructure evolution was studied at the center and edge of the HPT-processed discs using X-ray diffraction line profile analysis (XLPA) and transmission electron microscopy (TEM). Si addition altered the predominant plasticity mechanism from micro-band formation to extensive occurrence of nano-twinning at the early stage of HPT processing. At later stages of HPT processing, both alloys exhibited deformation twinning but its propensity was considerably higher for the Si-added MPEA, as revealed by ~50% higher twin fault probability. Additionally, the Si-added MPEA showed ~30% higher dislocation density at any given stage of HPT processing compared to the Si-free MPEA. A significantly accelerated nano-structuring coupled with a finer saturation grain size was observed in the Si-added MPEA (34 nm for Si-free versus 23 nm for Si-added). These effects can be explained by the influence of Si addition on lowering the stacking fault energy (SFE) (from ~40 mJ/m^2 in Si-free to ~20 mJ/m^2 in Si-added MPEA) and increasing the solute pinning effect of Si on lattice defects. The plasticity mechanisms at nano-scale were also influenced by the presence of Si as confirmed by the formation of nano-twins and stacking faults inside the nano-grains for the Si-added and Si-free MPEAs, respectively. The differences in plasticity mechanisms and microstructure evolution resulted in enhanced hardness in the early stages of HPT processing for the Si-added MPEA, but the difference in hardness between the two alloys tended to be reduced at higher strains.

---

* Corresponding author at: Academy of Scientific and Innovative Research (AcSIR), Ghaziabad 201002, India.
** Corresponding author.
E-mail addresses: avanish@nmlindia.org (A.K. Chandan), jeno.gubicza@ttk.elte.hu (J. Gubicza).

[1] These authors contributed equally to this work.

https://doi.org/10.1016/j.ijplas.2023.103720
Received 17 April 2023; Received in revised form 15 July 2023;

1. Introduction

High entropy alloys (HEAs) have led to a surge in multi-principal element alloy (MPEA) concepts leading to the discovery of novel alloys with outstanding mechanical and functional properties (Yeh et al., 2004; Cantor et al., 2004; Ding et al., 2018; Li et al., 2016; Ming et al., 2019; Miracle and Senkov, 2017; Schuh et al., 2018; Tong et al., 2019). Especially, in the context of face-centered cubic (FCC) high entropy and medium entropy alloys (MEAs), there have been reports regarding the achievement of unprecedented structural properties through innovative alloy design (Liu et al., 2022a; Jiang et al., 2022; Luo et al., 2020). Recently, CoCrNi MEA has been shown to possess the highest ever fracture toughness in a near-liquid helium environment (20 K) (Liu et al., 2022a). Such a remarkable damage tolerance of CoCrNi alloy was attributed to the sequential activation of deformation twinning and transformation-induced plasticity (TRIP) effects. Another FCC HEA, $Al_{0.1}$CoCrFeNi, showed an excellent work-hardening ability during high-strain rate tension tests which was attributed to a series of plasticity mechanisms namely nanoscale TRIP and symbiotic amorphization (Jiang et al., 2022). CoNiV FCC MEA was shown to be hydrogen-resistant which underwent a minimal reduction in tensile strength and ductility after exposure to the hydrogen environment due to low hydrogen diffusivity and activation of deformation twinning (Luo et al., 2020). Recently, Han et al. (2021) achieved a unique combination of soft magnetism and high strength-ductility balance in a CoFeNiTaAl HEA through uniform dispersion of coherent and ordered nanoprecipitates of $<$15 nm size in the FCC matrix. A simultaneous improvement in strength and ductility has been reported at strain rates $>$ 1000 s^{-1} for NiCoCrFe HEA stemming from nano-scale twinning, short-range ordering/ clustering, and phonon drag effect of dislocations (Zhang et al., 2020). Likewise, the presence of deformable kappa phase in a FCC MEA, CoNiV, is shown to simultaneously improve strength by shearing action and ductility by raising the flow stress close to the critical stress for twinning so that dynamic twinning promoted additional strain hardening (An et al., 2023).

Apart from the strategic alloy design, deploying suitable processing techniques to achieve refined microstructure down to nanometer size can result in further enhancement in properties and unique functionality (Shahmir et al., 2023), including strength-ductility synergy (Sathiyamoorthi et al., 2019), room temperature, and/ or high strain-rate superplasticity (Nguyen et al., 2020), remarkable fatigue strength (Renk et al., 2022) and inverted magnetism (Paul et al., 2023). Recently, FeCoNiCrCu HEA film via magnetron sputtering followed by annealing revealed the highest reported yield strength (3.4–4.2 GPa) under micro-compression compared to any single-phase FCC materials. Such a remarkable strength-plasticity synergy was attributed to grain boundary strengthening coupled with enhanced twinnability due to nano-scale chemical fluctuations (Zhang et al., 2021).

Various severe plastic deformation (SPD) techniques can yield superior microstructural refinement compared to conventional metal working techniques (Edalati et al., 2022a). Among different SPD techniques, high-pressure torsion (HPT) is the most effective in terms of achieving the finest possible grain size in metallic materials (Zhilyaev et al., 2003). It is worth mentioning that the extent of grain refinement during HPT processing depends on both (i) processing parameters and (ii) material characteristics. There are several reports on the effect of processing parameters, namely, the applied compressive pressure (Zhilyaev et al., 2003), the number of turns (Jamalian et al., 2019; Gubicza et al., 2016), strain rate (Hohenwarter and Pippan, 2019; Edalati et al., 2022b), and processing temperature (Xie et al., 2010) on the extent of grain refinement of FCC alloys, some of which holds true for FCC MPEAs as well (Sonkusare et al., 2020; Heczel et al., 2017; Kishore et al., 2022; Wu et al., 2017; Moon et al., 2018).

In terms of material characteristics, stacking fault energy (SFE) and pinning effect of solute atoms on lattice defects are potentially the two most important features affecting the microstructural refinement in FCC alloys with comparable melting points. The solute effect can be quantified with solid solution strengthening (SSS), i.e., the hardening caused by the solute atoms. With regard to the role of SFE on the microstructure evolution during HPT processing, there is a significant debate. For instance, Edalati et al. (2014) showed that there is no correlation between normalized grain size after HPT processing, d/b (d is the grain size after HPT and b is the magnitude of Burgers vector), and normalized SFE, SFE/Gb (G is shear modulus) for a wide range of pure metals and binary alloys. In contrast, Mohamed and Dheda (2012) demonstrated that the saturation grain size is dependent on the SFE of the material, and the lower the SFE, the finer the grain size. A similar observation was made for Cu-Al alloys (Shi et al., 2022). However, with respect to FCC MPEAs, there is no dedicated work on understanding the role of SFE on the extent of grain refinement and examining the underlying deformation mechanism(s) during the HPT processing. In terms of the role of SSS, it is widely accepted for conventional alloys that the higher the SSS, the finer the saturation grain size (Bruder et al., 2018; Pippan et al., 2010). However, in the context of FCC MPEAs, there is a lack of dedicated work on discerning the exact role of SSS on sequential grain refinement during HPT.

Few works allude to the role of alloy design in altering the plasticity mechanism(s) and grain refinement in FCC MPEAs during HPT. For instance, Chandan et al. (2022) showed the defining role of Ni addition to FeMnCoCr HEA on altering the predominant plasticity mechanism from TRIP to deformation twinning + dislocation glide during HPT processing. Gubicza et al. (2019) compared the extent of grain refinement in HPT-processed CoCrFeNi and CoCrFeMnNi MPEAs having comparable SFEs. CoCrFeMnNi alloy showed ~3 times finer saturation grain size than CoCrFeNi alloy owing to greater lattice distortion in the former. Keil et al. (2021) investigated the effect of SSS on the saturation grain size in a series of alloys varying from 142 nm in pure Ni to 55 nm in Cantor alloy. They concluded that the minimum achievable grain size after HPT processing is inversely proportional to the SSS. However, they ignored the possible role of SFE alteration by changing the material from pure Ni (high SFE: 125 mJ/m^2 (Hirth and Lothe, 1982)) to Cantor alloy (medium to low SFE: 30 ± 5 mJ/m^2 (Filho et al., 2022)) on grain refinement and its mechanisms. Thus, from the above discussions, it is evident that the role of alloying in grain refinement extent and plasticity mechanism(s) in FCC MPEAs should be examined in terms of both SFE alteration and SSS.

In the context of the role of alloying elements on the mechanical behavior of FCC MPEAs, Si is a fascinating element that alters the properties in an unexpected manner. Yamanaka et al. (2021) showed that while both Si and Ti addition to CoCrFeMnNi-based HEA led

Table 1
Summary of the chemical composition of Si-free and Si-added MPEAs (all concentrations are in atomic %).

Alloy	Co	Cr	Ni	Mn	Si	Fe
Si-free MPEA (Target)	33	19	33	15	–	–
Si-free MPEA (Actual)	32.86	18.67	32.79	15.35	–	0.33
Si-added MPEA (Target)	33	19	33	10	5	–
Si-added MPEA (Actual)	32.80	18.11	33.96	9.73	5.15	0.25

to an enhanced yield and tensile strength, Ti addition resulted in a loss of ductility, whereas Si addition led to an enhanced ductility as well. However, the mechanism of deformation was not studied to explain this intriguing behavior. Liu et al. (2020) studied the effect of Si content on phase stability and tensile behavior of CoCrNi MEA. They observed that with an addition of Si up to 6.25 at.%, single-phase FCC structure is retained, whereas ~9 at.% Si addition to CoCrNi alloy, resulted in a phase decomposition to sigma phase and another CrSi-rich phase. Interestingly, in the solid solution regime, there was a significant increase in both yield strength and tensile strength without a loss of ductility. Strengthening due to Si-addition was attributed to enhanced Hall-Petch effect and SSS arising from local lattice distortion around Si atoms. A recent work by Li et al. (2022) revealed that the deformation structure formed during cold rolling of Si-added CoCrNi alloy is finer compared to the well-studied Si-free CoCrNi alloy. Further, they achieved a remarkable cryogenic tensile property with UTS > 1.5 GPa, while maintaining a fair ductility of 20% in a hetero-structured Si-added CoCrNi MEA. Likewise, a small addition of Si (0.2 wt.%) in FeCrAl system helps in reducing the enthalpy of the formation of AB_2 type Laves phase and attaining its fully coherent precipitation in the matrix (Liu et al., 2022b). It is evident from these discussions that Si addition to FCC MPEAs has immense potential of improving their mechanical properties with the activation of intriguing deformation mechanisms.

Despite the availability of the aforementioned literature on the role of Si on microstructure evolution and mechanical properties during tensile deformation, there are no reports on the effect of Si addition on the HPT response of FCC HEAs/ MEAs. It is well-established that HPT processing can result in unexpected deformation mechanism(s) and phase transition compared to tensile or compressive tests (Chandan et al., 2021a; Liu et al., 2021) and hence there is a fundamental need to understand the effect of Si on microstructure evolution and plasticity mechanism(s) during HPT processing. With this motivation, we fabricated two model MPEAs, viz., Si-free ($Co_{33}Ni_{33}Cr_{19}Mn_{15}$) MEA and Si-added ($Co_{33}Ni_{33}Cr_{19}Mn_{10}Si_5$) HEA. Deliberately, we added 5 at.% Si to study the effect of Si addition in the single-phase solid solution regime without any phase decomposition on the HPT-induced plasticity mechanisms. In this work, we have addressed the following research questions regarding the role of Si addition in CoCrNiMn MEA:

(i) Effect of Si addition on the SFE and lattice distortion in the studied FCC MPEA.
(ii) Whether Si alters the plasticity mechanisms, such as slip, TWIP, TRIP, and grain boundary mediated deformation during HPT.
(iii) If Si influences the mechanism(s), kinetics, and extent of grain refinement during HPT.
(iv) If the plasticity mechanism(s) and ensuing microstructure are affected only at the early stage of HPT processing or the effect is sustained over the larger strain as well.
(v) Whether Si affects the strengthening mechanism(s) during HPT.

Additionally, we investigated the applicability of conventional strengthening models for the two studied HPT-processed CoCrNiMn MPEAs with and without Si.

2. Materials and methods

2.1. Fabrication of Si-free and Si-added medium entropy alloys

Co, Ni, Cr, Mn, and Si having a purity of at least 99.9 wt% were used as the starting raw materials for vacuum induction melting to achieve the targeted alloy compositions. The actual composition of the cast ingots was determined using X-ray fluorescence spectroscopy. Table 1 provides the chemical composition of the Si-free and Si-added MPEAs. Compared to the Si-free MPEA, the actual composition of the Si-added MPEA had ~5 atomic % of Si. Both the alloys contained unintentional addition of Fe as an impurity element in < 0.5 atomic %. It is worth noting that the chemical composition of both the alloys with respect to Co, Cr, Ni and Fe are comparable, whereas there is a partial replacement of 5 atomic % Mn by Si in the Si-added MPEA. From the viewpoint of alloy design, it is expected that the addition of Si to the Cantor alloy and its subclass would lead to a reduction in the SFE (Chang et al., 2021). Likewise, a lowering of Mn content has the same effect on the SFE (Kishore et al., 2022).

The cast ingots were homogenized at 1200 °C for 1.5 h. Subsequently, ingots having a dimension of $50 \times 50 \times 75\ mm^3$ were sectioned to a dimension of $25 \times 50 \times 75\ mm^3$. The sectioned ingots were then forged at 1100 °C to break the cast structure and to achieve a plate having a thickness of 12 mm. It was followed by hot rolling at 1000 °C and cold rolling to achieve a sheet thickness of 2 mm. Then, annealing was conducted at 900 °C for 45 min, followed by instant water quenching to prevent any possibility of precipitation. HPT specimens were prepared from these sheets by taking out discs of 10 mm diameter and reducing the thickness of these discs to 0.9 mm by polishing using emery papers of 600 grit size to achieve a similar surface roughness.

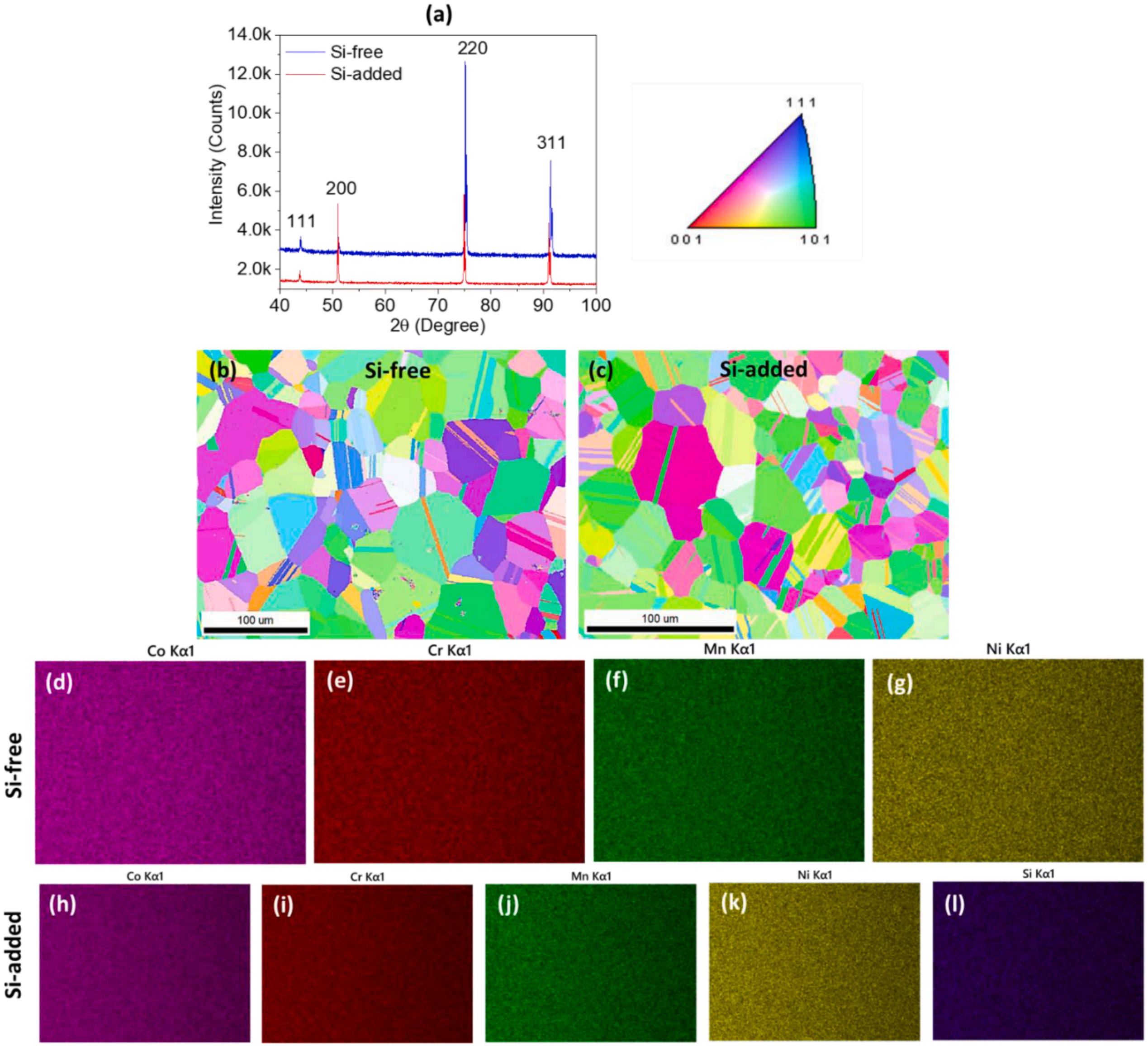

Fig. 1. Initial microstructure of the studied MPEAs: (a) XRD patterns of Si-free and Si-added MPEAs showing the presence of FCC phase; Inverse pole figure map of (b) Si-free, (c) Si-added MPEAs; EDS maps of (d–g) Si-free, and (h–l) Si-added MPEAs.

2.2. High-pressure torsion experiments

In this work, HPT experiments were conducted in a quasi-constrained set-up. disk specimens were placed between an upper and a lower anvil and 6 GPa pressure was applied. This was followed by a rotation of the anvil at 1 rpm. Both sets of alloys were subjected to 0.5 turn and 5 turns of rotation. More detail about the quasi-constrained HPT set-up and processing can be found in previous works (Chandan et al., 2022; Kawasaki et al., 2011).

2.3. Materials characterization before and after HPT processing

Microstructure characterization of the specimens before HPT processing consisted of X-ray diffraction (XRD) for determining the crystal structure and lattice parameters of Si-free and Si-added MPEAs, electron backscattered diffraction (EBSD) for estimation of grain sizes and bulk texture analysis using XRD. All the analyses were done on the rolling plane, that is, the plane of the HPT disk. The investigation of microstructure after HPT processing was conducted at two different locations, namely, the center and edge. The edge location is referred to as 4 mm away from the disk center. A standard metallographic procedure for sample preparation involved polishing with silicon carbide emery papers starting with a grit size of 120 and successively increasing up to 4000. This was followed by polishing using colloidal alumina suspension of 1 μm size. Afterward, samples were electropolished using a solution of 70% methanol, 20% perchloric acid, and 10% glycerin with a Struers Lectropol-5 at 14 V for 10 s.

The XRD measurements were performed at the center and edge locations of the HPT-processed discs by employing a Smartlab diffractometer (manufacturer: Rigaku, Japan) in θ-θ geometry with parallel beam and CuKα_1 radiation (wavelength, λ=0.15406 nm). The 2θ angle range for the XRD measurements was 35–105° for all specimens. A beam with the following dimension was utilized: length = 2 mm and width = 0.25 mm. The lattice constants were determined from the peak positions using the Nelson-Riley method (Nelson and Riley, 1945). Williamson-Hall plots were prepared for an easy qualitative recognition of the effect of number of HPT turns, location on the disk surface (center or edge) and Si addition on X-ray peak broadening. On a Williamson-Hall plot, the peak breadth in the reciprocal space for the available diffraction peaks is plotted as a function of the magnitude of the diffraction vector $\left(K = \frac{2sin\theta}{\lambda}\right)$, where θ and λ are the diffraction angle and the wavelength of X-ray, respectively (Williamson and Hall, 1953). The peak breadth (ΔK) can be obtained from the full width at half maximum (FWHM) as $\Delta K = \cos\theta \cdot \Delta(2\theta)/\lambda$ where $\Delta(2\theta)$ is the FWHM of the peak.

A procedure of convolutional multiple whole profile (CMWP) fitting was used to perform X-ray diffraction line profile analysis (XLPA) in order to discern the values of various microstructural parameters such as crystallite (or diffraction domain) size, dislocation density, twin fault probability etc. which evolve during HPT processing (Gubicza, 2014). This method involves the fitting of the diffraction pattern by the sum of a background spline and the theoretical peak profiles. The theoretical peak profiles were attained as the convolution of the calculated line profiles (which are related to crystallite size, dislocations and twin faults) and the instrumental peak. Since the massive plastic deformation during HPT processing resulted in a much higher peak broadening than the instrumental effect, the present study did not involve instrumental correction. The CMWP fitting yielded the dislocation density (ρ) and the area-weighted mean crystallite size ($<x>_{\mathrm{area}}$) where the later quantity was deduced from the log-normal variance of the crystallite size distribution (σ^2) and the median (m) as $<x>_{area}=m\cdot exp(2.5\sigma^2)$. In addition, the twin fault probability (β) was also obtained by CMWP fitting. The quantity gives the fraction of {111} planes containing twin faults. A more detailed description of the CMWP method can be found elsewhere (Ribárik et al., 2004).

The microstructural examination was further conducted using transmission electron microscopy (TEM). Preparation of TEM specimens from HPT-processed specimens consisted of mechanical thinning to achieve a sample thickness of ~50–60 μm. Subsequently, Gatan's dimple grinder was employed to further thin down the samples up to the thickness ~15–20 μm. This was followed by further thinning the samples employing Gatan's PIPS II equipment to make the specimen electron transparent. In order to avoid ion milling induced artifact generation, a cold sample stage was used for slow and controlled milling of the samples. Finally, plasma cleaning of the samples was done before the TEM investigation. TEM investigation was performed employing JEOL's 200 kV JEM 2200FS equipment.

To establish microstructure-property correlation in HPT-processed specimens, hardness measurements along 6 different diameters of the discs were performed using a Vickers hardness testing machine (EMCO). Hardness values were measured at a load of 500 g with a dwell time of 30 s. The average hardness of 6 measurements for a particular location (distance from the center of the disk) along with standard deviation is reported.

3. Results

3.1. Effect of Si addition on the initial microstructure

Fig. 1(a) shows the XRD pattern of Si-free and Si-added MPEAs. Sharp diffraction peaks corresponding to (111), (200), (220), and (311) planes of an FCC structure were observed for both alloys. These diffractograms suggest that an addition of 5 at.% Si did not lead to phase decomposition and the single-phase FCC crystal structure was retained. The XRD peak positions of Si-added MPEA were slightly shifted towards the higher 2θ indicating a reduction in interplanar spacing (d). The addition of Si reduced the lattice parameter of the FCC structure from 3.581 to 3.573 Å, which was expected owing to the smaller size of Si atoms compared to the mean size of Co, Cr, Ni, and Mn atoms.

The microstructure of the Si-free and Si-added alloys represented in form of inverse pole figure (IPF) maps before HPT processing

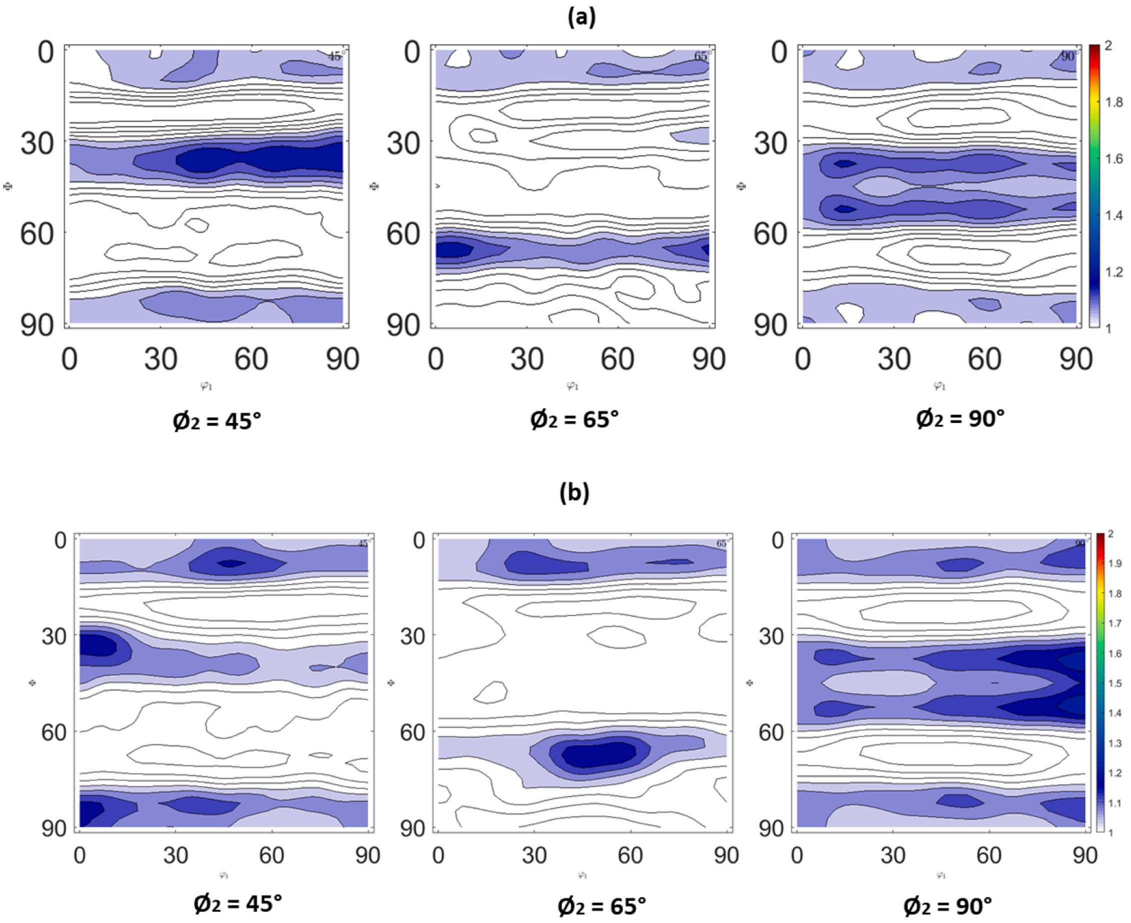

Fig. 2. Bulk texture of specimens prior to HPT processing represented using orientation distribution functions (ODFs) with ϕ_2 sections at 45°, 65°, and 90° for: (a) Si-free MPEA, and (b) Si-added MPEA.

are shown in Fig. 1(b) and (c), respectively. Both alloys consisted of polygonal FCC grains with annealing twins. The average grain sizes (excluding annealing twins) for the Si-free and Si-added MPEAs measured using the line intercept method were determined to be 38 μm and 32 μm, respectively. The addition of Si led to a slight reduction in the grain size despite adopting a similar thermomechanical processing. This may be due to the solute drag effect limiting the migration of high-angle grain boundaries (Shah et al., 2020). A similar effect of Si on grain refinement of another FCC HEA system has been reported previously (Liu et al., 2020). A higher fraction of annealing twins (defined as % length of twin boundaries among the grain boundaries) was observed in the Si-added alloy (62.3%) compared to the Si-free alloy (56%), which possibly indicates a reduction of stacking fault energy (SFE) due to Si addition (Chang et al., 2021). In terms of homogeneity of chemical composition, both alloys showed a uniform distribution of constituent elements without any evidence of elemental segregation as shown in Fig. 1 (d–g) and 1 (h–l) for the Si-free and Si-added MPEAs, respectively. Further, orientation distribution function (ODF) sections with ϕ_2 sections at 45°, 65° and 90° of the Si-added and Si-free MPEAs shown in Fig. 2 (a) and (b), respectively, revealed a very weak crystallographic texture and hence precluding their significant role in the deformation mechanism(s) during HPT processing.

In addition to the notable changes in grain size and lattice parameter of the Si-added FCC MPEA, the addition of the much smaller Si atoms is also expected to induce a greater lattice distortion. To quantify the extent of lattice distortion (δ) in the Si-free and the Si-added MPEAs, the following equation is used:

$$\delta = \left[\sum_{i=1}^{n} c_i \left(1 - \frac{r_i}{\bar{r}} \right)^2 \right]^{0.5}, \tag{1}$$

where $\bar{r} = \sum_{i=1}^{n} c_i r_i$, c_i and r_i are the molar fraction and atomic radius of the ith element and n is the number of elements in the alloy. Clearly, $\delta_{\text{Si-added}}$ is 0.0189 compared to $\delta_{\text{Si-free}} = 0.0122$ which means an addition of Si resulted in ~50% increase in the lattice distortion.

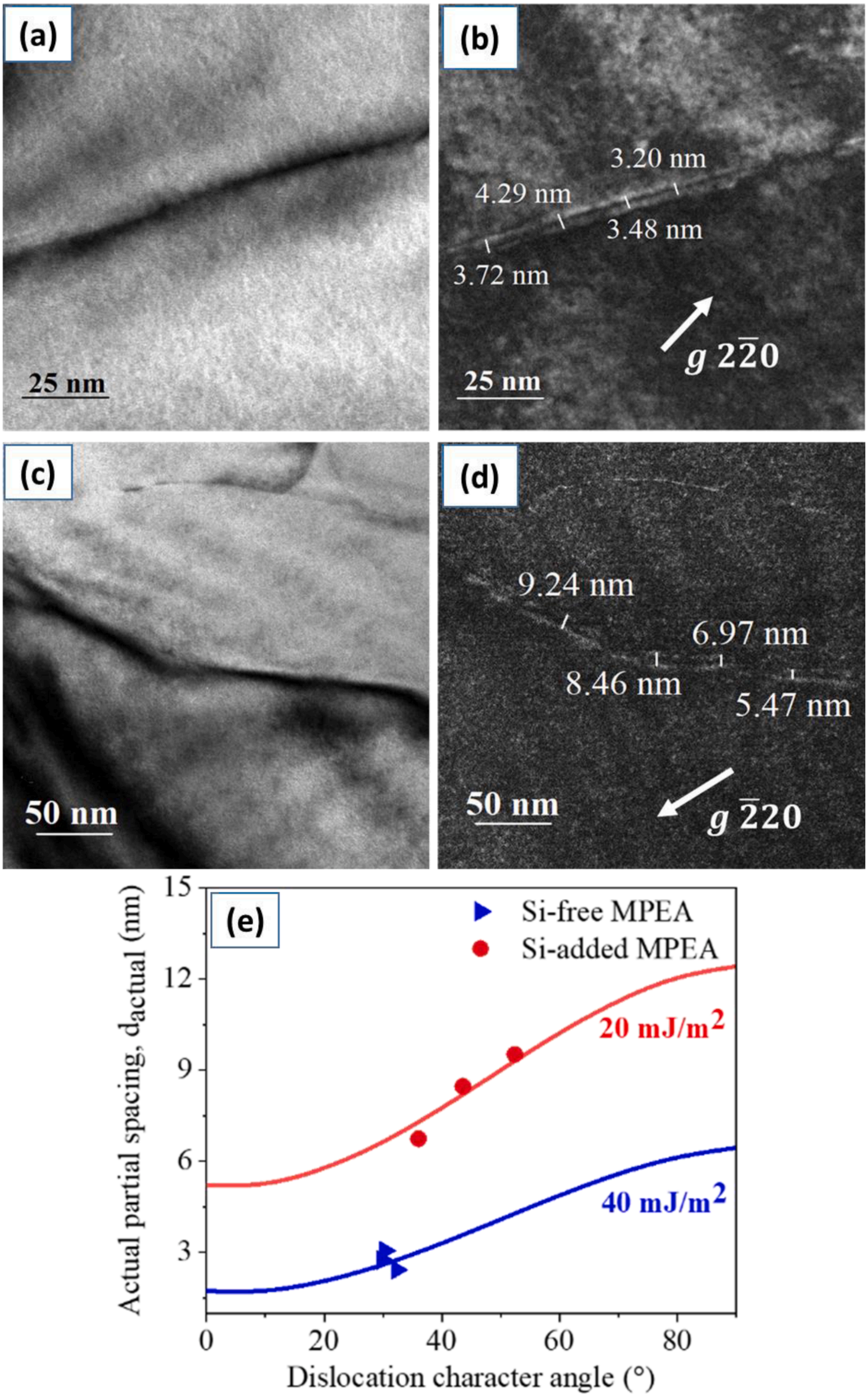

(caption on next page)

Fig. 3. TEM BF micrograph showing a dislocation in the tensile-deformed (at the engineering strain of 3%) Si-free MPEA, (b) the corresponding WBDF micrograph depicting the distinct contrast between the Shockley partial dislocation pair, (c) TEM BF micrograph showing a dislocation in the tensile-deformed (at the engineering strain of 3%) Si-added MPEA, (d) the corresponding WBDF micrograph depicting the distinct contrast between the Shockley partial dislocation pair; Some measured partial spacing values are shown in (b) and (d), and (e) theoretical partial dislocation spacing vs dislocation character angle curves for the Si-free and Si-added MPEAs with the experimental data overlaid in the same.

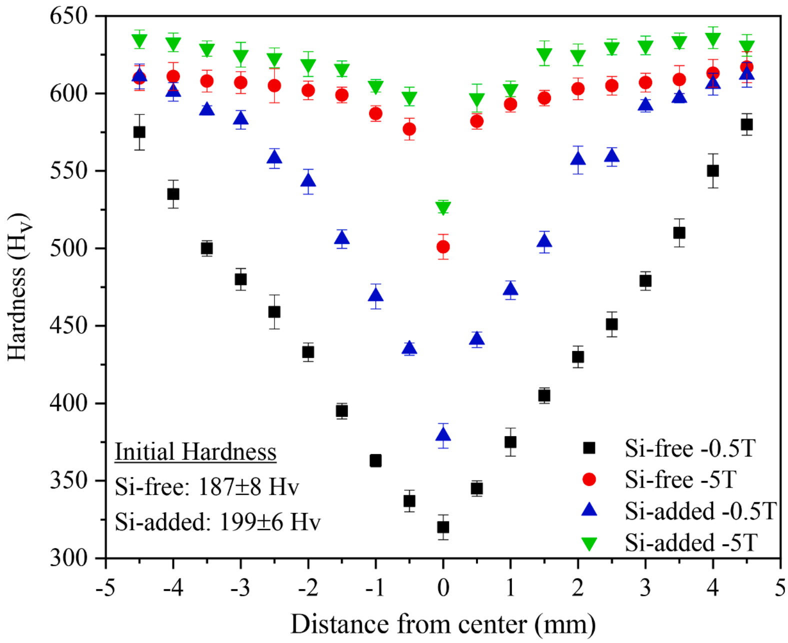

Fig. 4. Evolution of hardness profile along the diameter of the disk due to HPT processing of Si-free and Si-added MPEAs.

3.2. Effect of Si addition on SFE

In Section 1, we presented a brief overview on the possible role of SFE on the grain refinement during HPT processing of various alloys. Furthermore, SFE also affects the deformation behavior of the FCC phase (Chandan et al., 2021b; Laplanche et al., 2017; Wang et al., 2018). The MPEAs under study were produced with the aim of changing the lattice distortion and SFE due to the variation of Si and Mn contents. In this section, we estimate the SFE of the MPEAs under study. As the first step, the MPEAs were deformed under tension up to 3% engineering strain to form dissociated dislocations in the microstructure (Laplanche et al., 2017). This was followed by microstructural characterization employing TEM. An estimation of the SFE was carried out using the following relationship between the SFE and the spacing between the Shockley partial dislocations (d) assuming an isotropic elasticity (Hirth and Lothe, 1982):

$$SFE = \frac{Gb_p^2}{8\pi d(1-\nu)}(2-\nu-2\nu cos2\beta), \tag{2}$$

where G and ν are the shear modulus and the Poisson's ratio, respectively (values given in Appendix A1); β is the angle between the Burgers vector and the line vector of lattice dislocation and b_p is the magnitude of Burgers vector of the partial dislocations. b_p is given as: $\left(\frac{a_0}{6}\langle 112\rangle\right)$, where a_0 is the lattice parameter of the MPEAs and the same was obtained from XRD measurements (values given in Section 3.1). The measurement of the values of d and β was performed from weak beam dark field (WBDF) micrographs formed under the $\langle 111\rangle$ zone axis (ZA) with the $\langle 220\rangle$ type active diffraction vector (g). Fig. 3(a) and (c) present TEM bright field (BF) micrographs of dissociated dislocations in which partials could not be resolved in the two-beam diffraction conditions for the Si-free and Si-added MPEAs, respectively. The corresponding WBDF micrographs could discern the spacing between the partial dislocations as demonstrated in Fig. 3(b) and (d) for the Si-free and Si-added MPEAs, respectively. It is evident that the distance between the Shockley partials increased significantly in the Si-added MPEA, indicating a decrease in SFE of the same compared to the Si-free MPEA (as per Eq. (2)). Measurement of d was carried out along the straight segment of the isolated partial dislocations in an interval of at least 15 nm in the WBDF micrographs. As the actual position of the dislocation cores is influenced by the dislocation depth within the foil, foil thickness and excitation error (Cockayne, 1972; Cockayne and Vitek, 1974), the measured dislocation widths were corrected to obtain the actual dislocation separation distance (as shown in Appendix A2) before its application in Eq. (2). The appearance of both partial dislocations in the images (see Fig 3(b) and (d)) suggests that $|g.b_p| = 1$ for both partial dislocations at only one g vector and in this condition, the Burgers vector is parallel to the g vector. Accordingly, the dislocation character angle (β) was measured as the angle

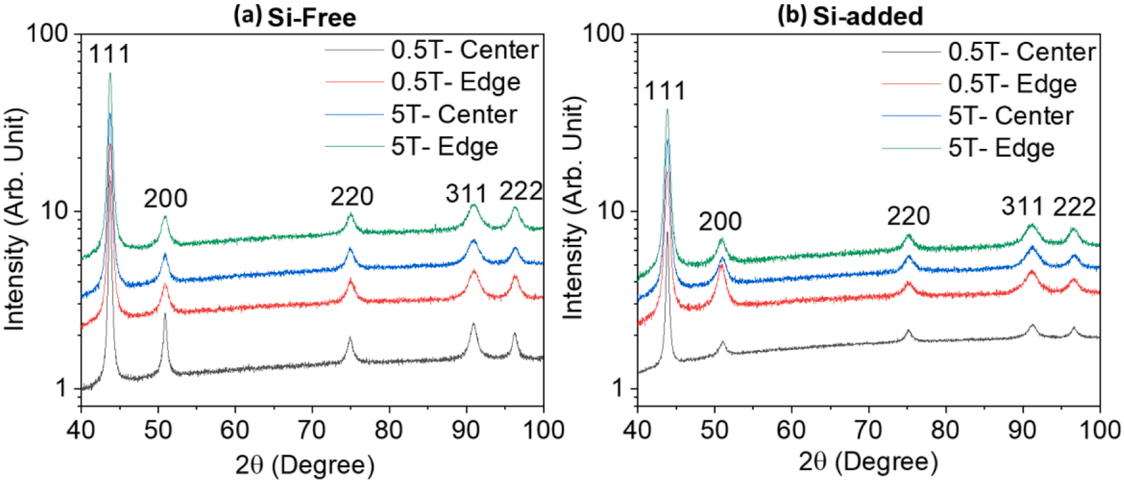

Fig. 5. XRD patterns acquired from the center and edge locations of HPT- processed specimens after 0.5 and 5 turns: (a) Si-free MPEA, (b) Si-added MPEA.

between the dislocation line vector and the *g* vector. Fig. 3(e) presents the theoretical partial dislocation spacing versus dislocation character angle curves for the studied MPEAs (Aerts et al., 1962) with the corresponding experimental data overlaid in the same. The addition of Si and along with the reduction in the Mn content from the Si-free alloy to form the Si-added alloy resulted in the decrease in SFE from ~40 mJ/m^2 in the Si-free MPEA to ~20 mJ/m^2 in the Si-added MPEA.

3.3. Hardness evolution due to HPT processing

The evolution of the hardness along the diameter of the disk due to HPT processing of the Si-free and Si-added MPEAs is shown in Fig. 4. Prior to HPT processing, the average hardness of the Si-added MPEA was 12 Hv greater than the Si-free MPEA. Such a small increase in hardness due to Si addition can be attributed to the (i) greater lattice distortion (δ (Zhang et al., 2008)) caused by the smaller Si atoms ($\delta_{\text{Si-added}}$: 0.0189 versus $\delta_{\text{Si-free}}$: 0.0122) resulting in solid solution strengthening, and (ii) slightly finer initial grain size. HPT processing to 0.5 turn (0.5T) led to a remarkable increase in the hardness of the disk in both alloys.

An increase in hardness with an increasing distance from the center of the disk ($r = 0$) is noted for both alloys. This is consistent with earlier reports on hardness evolution during HPT processing of medium-to-low SFE FCC alloys such as austenitic stainless steels and Cantor alloy and its subsets (Chandan et al., 2022; Gubicza et al., 2019; Shahmir et al., 2016; Zhao et al., 2021). Such an increasing trend of hardness evolution from the disk center towards its edge is common for many alloys (Kawasaki, 2014) and is explained based on location-dependent shear strain (γ) in the disk during HPT processing given by the following equation (Zhilyaev et al., 2003):

$$\gamma = 2\pi \mathrm{rn} / \mathrm{t}, \tag{3}$$

where *r* is the distance from the center of the disk, *n* is the number of turns of HPT processing, and *t* is the thickness of the HPT-processed specimen. Clearly, for a fixed number of turns of HPT processing (*n*), the shear strain increases with an increasing distance from the center of the disk (*r*). Based on Eq. (3), the shear strain at the center of the disk should be zero and hence there should not be any hardening at the center. However, in practice, a significant hardening is observed even at the center of the disk for even 0.5 turn of HPT processing. For instance, in the Si-free and Si-added MPEAs, the hardness increased from ~187 Hv to ~320 Hv and ~199 Hv to ~380 Hv, respectively, at the center of the disk after 0.5 turn of HPT processing. The increase in the hardness at the center of the disk is variously attributed to a combination of factors, namely, compressive strain during HPT processing (Song et al., 2011), the quasi-constrained nature of HPT processing, where there is a finite plastic deformation of a disk between the anvils leading to a small outward flow of the material, and a finite non-zero value of the indentation area during hardness measurement which is not only measuring the hardness at the center of the disk but is also getting influenced by a small nearby region (Estrin et al., 2008; Huang et al., 2014). In addition, the disk center is surrounded by regions where there is a significant strain according to Eq. (3), and the formed lattice defects (such as dislocations) have a stress field even in the center, resulting in an induced plastic deformation. Fig. 4 reveals that any given location, the hardness of the Si-added MPEA was substantially greater than the corresponding location of Si-free MPEA after 0.5 turn of HPT processing.

After 5 turns of HPT processing, some peculiar observations in hardness evolution were noted. These are: (i) at any given location of the HPT-processed disk, the hardness was higher for the Si-added MPEA compared to the Si-free MPEA; however, the difference in hardness between the two alloys was reduced compared to 0.5 turn of HPT processing, (ii) even after 5 turns of HPT processing, homogenization in hardness between center and edge of the disk was not fully achieved, while the difference in the hardness between the center and the edge locations became less considerable, (iii) a greater than three-fold increase in hardness compared to the unprocessed specimens was achieved at the edge location after 5 turns of HPT processing for both Si-free and Si-added MPEAs, and (iv)

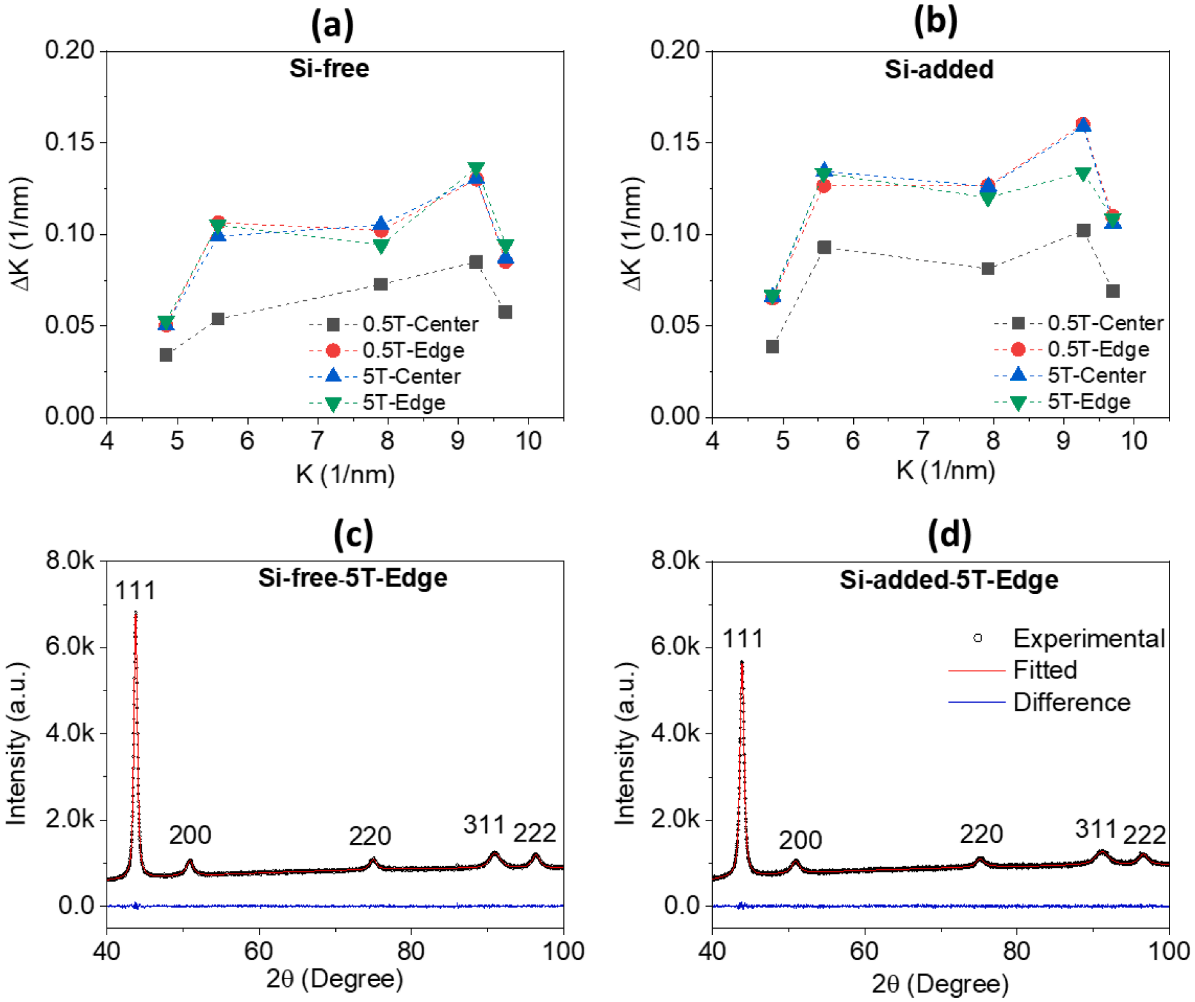

Fig. 6. Williamson-Hall plots for HPT-processed specimens for (a) Si-free, (b) Si-added MPEA; illustration of experimentally observed and CMWP-fitted XRD patterns for 5 turns HPT-processed specimen at edge locations of (c) Si-free, and (d) Si-added MPEAs.

the hardness achieved at the edge of the Si-free MPEA after 5 turns of HPT could be achieved after only 0.5 turn of HPT for the Si-added MPEA at its edge location.

3.4. Microstructural investigation through XLPA

During HPT processing of FCC alloys, distinct deformation mechanisms, namely, (i) dislocation glide, (ii) twinning, and (iii) FCC-to-HCP or FCC-to-BCC phase transformation also referred to as TRIP effect, and (iv) grain boundary mediated strain accommodation are variously reported (Chandan et al., 2022; Gubicza et al., 2019; Keil et al., 2021). Akin to the conventional alloys, FCC MPEAs have also shown to largely obey the SFE-deformation mechanisms correlation during conventional processing, viz., the prominent deformation mechanism is dislocation glide for high SFE, deformation twinning for medium SFE and TRIP for low SFE alloys (Chandan et al., 2021b; Laplanche et al., 2017; Wang et al., 2018). As shown in Fig. 5(a) and (b), both Si-free and Si-added alloys showed single-phase FCC structure after 5 turns of HPT processing at both center and edge locations. As in the present case, HPT processing involved an application of a very high pressure of 6 GPa and an extremely high shear strain (~180 at the edge of 5 turns HPT-processed specimen), an absence of any notable phase transformation indicates a very high mechanical stability of the FCC phase in both alloys. Further, this ascertained that the TRIP effect cannot be the dominant plasticity and strengthening mechanism in either of these alloys during HPT processing.

Fig. 6(a) and (b) show the Williamson-Hall plots of the HPT-processed Si-free and Si-added MPEAs, respectively. Anisotropic peak broadening ($\Delta K = \cos\theta \cdot \Delta(2\theta)/\lambda$ where $\Delta(2\theta)$ is the FWHM of the peak) as a function of the magnitude of the diffraction vector ($K = 2\sin\theta/\lambda$) was observed for the studied MPEAs. This was an indication of peak broadening due to the accumulation of dislocations and refinement of crystallite size. Further, for both Si-free and Si-added MPEAs, the peak broadening at the disk center after 0.5 turn was

Table 2
The microstructural parameters obtained by XLPA for Si-free MPEA in different HPT-processed conditions.

HPT turn / Location	Diffraction domain size [nm]	Dislocation density [10^{14} m^{-2}]	Twin fault probability [%]
1/2, center	31 ± 4	116 ± 14	0.3 ± 0.1
1/2, edge	23 ± 3	250 ± 30	1.2 ± 0.2
5, center	23 ± 3	270 ± 30	1.4 ± 0.2
5, edge	24 ± 3	280 ± 30	1.6 ± 0.2

Table 3
The microstructural parameters obtained by XLPA for Si-added MPEA in different HPT-processed conditions.

HPT turn / Location	Diffraction domain size [nm]	Dislocation density [10^{14} m^{-2}]	Twin fault probability [%]
1/2, center	37 ± 4	146 ± 16	1.5 ± 0.2
1/2, edge	19 ± 2	350 ± 40	2.1 ± 0.2
5, center	18 ± 2	360 ± 40	1.9 ± 0.2
5, edge	19 ± 2	370 ± 40	2.4 ± 0.3

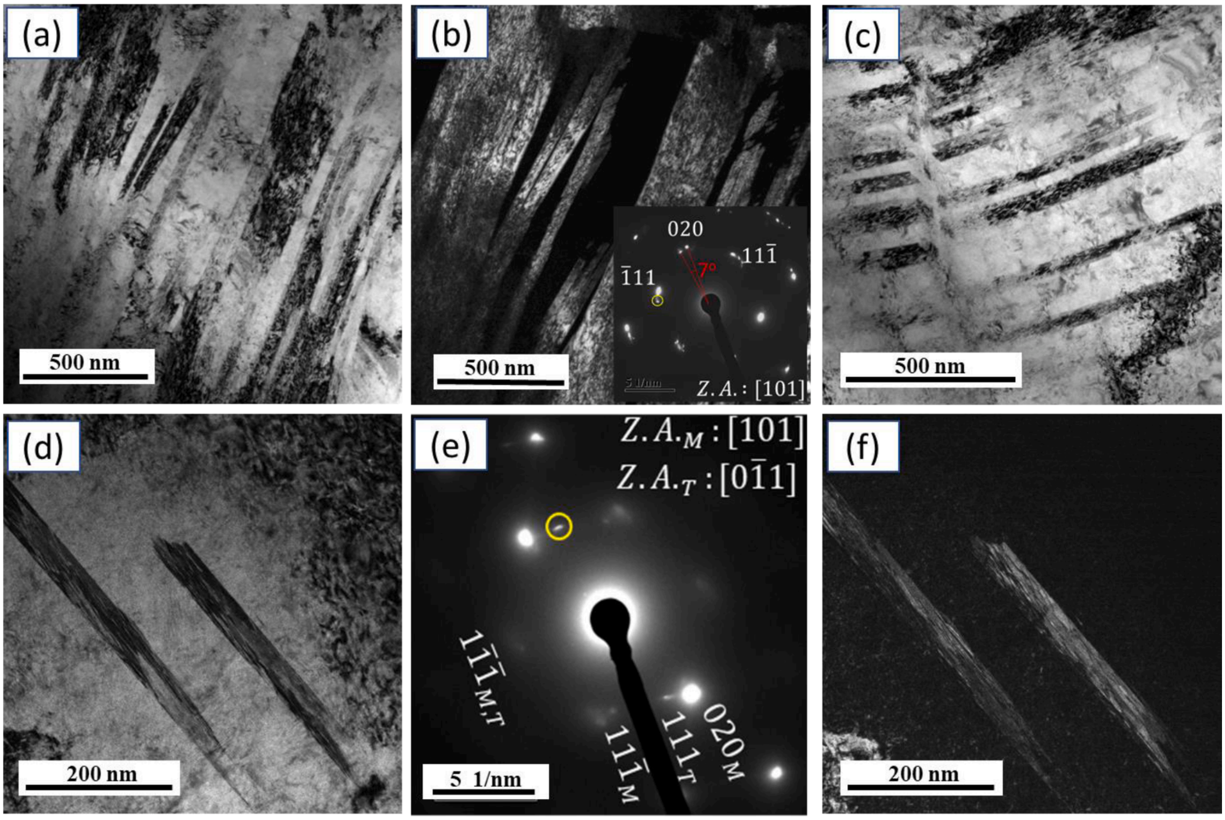

Fig. 7. Evidence of heterogenous deformation features at the center of 0.5 turn HPT-processed Si-free MPEA (a) BF TEM image showing micro-bands, (b) corresponding dark field (DF) image and indexed Selected area diffraction (SAD) pattern in the inset, (c) illustration of proliferation of micro-bands, (d) BF TEM image showing deformation twins, (e) corresponding SAD pattern, and (f) DF TEM of (d) imaged using the encircled diffraction spot in (e).

significantly smaller compared to the edge location, whereas for 5 turns of HPT processing, broadening at center and edge tend to be similar. Fig. 6(c) and (d) illustrate the CMWP fitting of XRD patterns corresponding to 5 turns HPT-processed specimens at the edges for the Si-free and Si-added MPEAs, respectively. An excellent match between the experimental and fitted patterns was evident from the nearly zero value of the difference between the two for each 2θ position for both the alloys. Similar fitting was obtained for both alloys in different HPT-processed conditions (not shown separately).

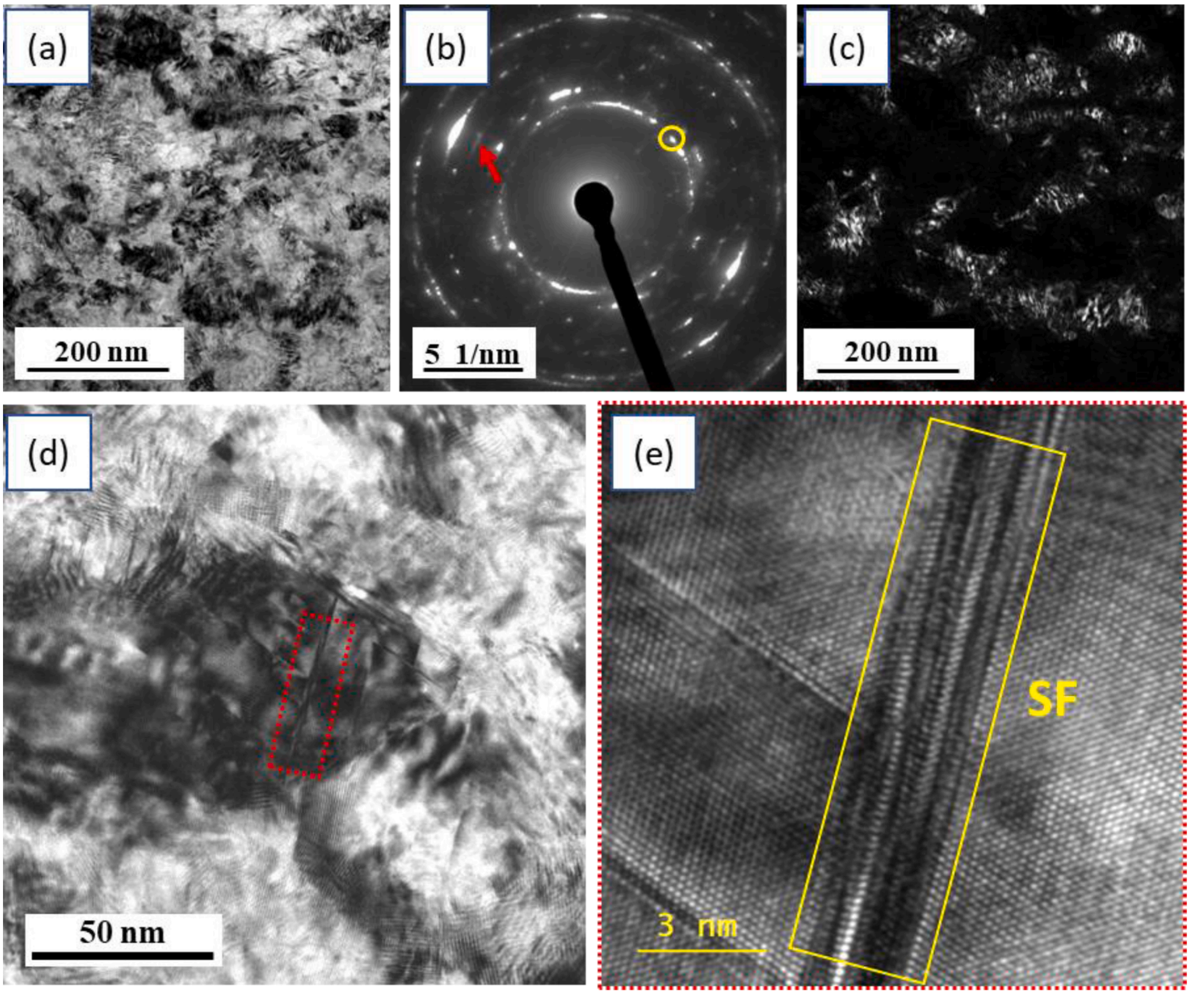

Fig. 8. TEM images of Si-free MPEA at the edge location after 0.5 turn of HPT processing (a) BF TEM image showing significant grain refinement, (b) corresponding SAD pattern, (c) DF TEM image produced using the encircled diffraction spot in (b), (d) high magnification BF TEM image showing planar faults, and (e) HRTEM image of the marked region in (d) depicting planar fault to be stacking faults.

Tables 2 and 3 summarize the microstructural parameters obtained using XLPA for the HPT-processed Si-free and Si-added MPEAs, respectively. The Si addition resulted in a significant increase in the density of lattice defects (dislocations and twin faults) formed during HPT while the change in the crystallite size was marginal for a given HPT processing condition. In line with the remarkable increase in the hardness at the center of the disk after 5 turns, a massive increase in dislocation density was achieved to reach the order of 10^{16} m^{-2} in both alloys. As indicated by the Williamson-Hall plots in Fig. 6, the difference in dislocation density between center and edge locations was significant after 0.5 turn by HPT but it tended to nullify after 5 turns for both the alloys. For the HPT-processed specimens after 5 turns, a saturation in dislocation density and diffraction domain size was observed for the Si-free and Si-added MPEAs. However, the dislocation density after 5 turns in the Si-added MPEA was ~33% greater than that in the Si-free MPEA. Moreover, after 5 turns of HPT processing, the diffraction domain size for the Si-added MPEA was only marginally smaller than the Si-free MPEA (23 ± 3 nm for Si-free MPEA versus 18 ± 2 nm for Si-added MPEA). Further, an addition of Si has resulted in a 50% increase in the twin fault probability at the edge of 5 turns of HPT processing. Remarkably, the twin fault probability at the location of maximum shear strain (viz., disk edge after HPT for 5 turns) in Si-free MPEA was achieved at the location of the minimum strain (viz., disk center after HPT for 0.5 turn) in the Si-added MPEA suggesting a very high tendency for deformation twinning in the Si-added MPEA, which is consistent with the significant reduction of the SFE in the Si-added MPEA.

3.5. Deformation mechanisms and grain refinement during HPT

3.5.1. Si-free MPEA

Highly heterogeneous deformation features were observed at the center of the 0.5 turn HPT-processed Si-free MPEA. While predominantly micro-bands as illustrated in Fig. 7 (a–c) were observed, evidence of the formation of deformation twins was also noted as

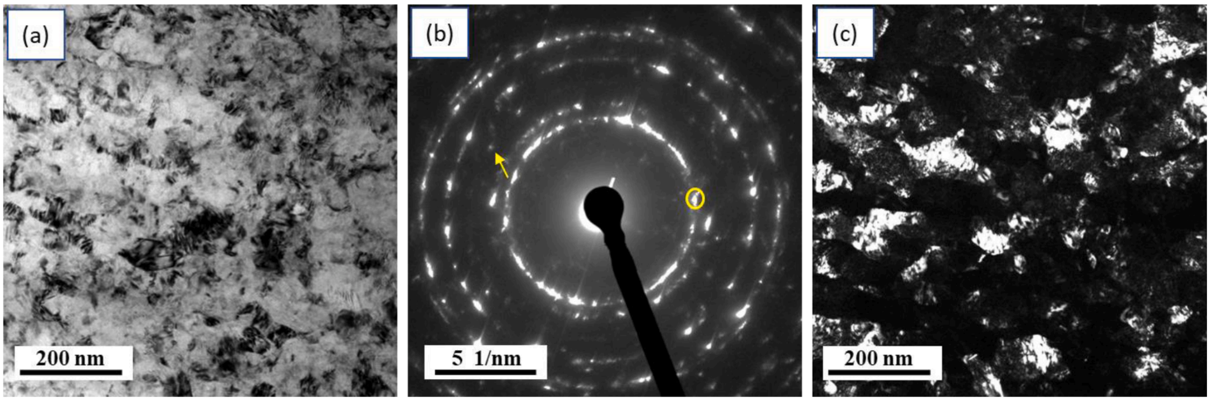

Fig. 9. TEM images of Si-free MPEA at the center of 5 turns HPT-processed specimen (a) BF TEM image showing appearance of nano-grains, (b) corresponding SAD pattern, and (c) DF TEM images produced using the encircled diffraction spot in (b) showing the large variation in the grain size distribution.

shown in Fig. 7 (d–f). The spacing between the micro-bands varied between 100 and 350 nm, whereas the mean spacing between deformation twins was ~130 nm. No indication of the formation of nano-structured grains was observed.

TEM micrographs of the Si-free MPEA at the edge location after 0.5 turn of HPT processing are shown in Fig. 8. Compared to the center of the disk after 0.5 turn, the edge location revealed extensive grain refinement. A representative BF image, corresponding SAD pattern and DF image are shown in Fig. 8 (a–c), respectively. A statistical analysis using ImageJ software considering more than 100 grains revealed an average grain size to be ~ 75 ± 43 nm. The tendency for nano-structuring which was yet to be fully achieved was evident from the incomplete ring in the SAD pattern (Fig. 8(b)). Additionally, the signature of the meager presence of the deformation-induced HCP phase was observed (faint presence of the (102) HCP reflection marked in Fig. 8(b)). The formation of planar faults in several nano-sized grains was also revealed as shown in Fig. 8(d). HRTEM image depicted the planar faults to be a bundle of stacking faults within the nano-structured grains as shown in Fig. 8(e).

TEM micrographs taken at the disk center of the 5 turns HPT-processed Si-free MPEA are shown in Fig. 9. Compared to the center of the 0.5 turn HPT-processed specimen, where micro-bands and deformation twins were observed, in this case, the formation of nano-grains is evident from the DF TEM image (Fig. 9(c)). Additionally, the SAD pattern shows a minor HCP phase appeared at the disk center after 5 turns (arrow in Fig. 9(b)). The average grain size was estimated to be 64 ± 40 nm. The nano-structuring in this case was incomplete as confirmed by the incomplete ring formation (Fig. 9(b)).

Microstructure at the edge of 5 turns HPT-processed Si-free alloy revealed extensive nano-structuring as shown in Fig. 10 (a–c). The average grain size was measured to be 34 ± 26 nm. Further, as shown in Fig. 10(c), nano-grains having fine deformation features were investigated through the HRTEM image shown in Fig. 10(d). Bundles of finely spaced stacking faults were observed within the nano-grains indicating a continued dislocation activity even after nano-structuring inside the grain. Generally, after extensive nano-structuring, grain boundary sliding is known to be one of the prominent deformation mechanisms but herein, we observed significant deformation in the form of stacking faults generation inside the nano-grains.

3.5.2. Si-added MPEA

TEM images from the center of the Si-added MPEA subjected to 0.5 turn of HPT processing revealed an extensive occurrence of deformation twinning as shown in Fig. 11. The mean twin spacing was measured to be ~20 nm, which was much finer than that observed at the corresponding location in the Si-free MPEA. A higher propensity of twinning in the Si-added MPEA was consistent with a significantly higher twin fault probability determined using XLPA and a lower SFE value. Further, there was an occurrence of hierarchical twinning: primary twinning followed by secondary twinning across them as shown in Fig. 11(d). Such twin-twin intersections sub-divided the microstructure significantly.

The edge location of the Si-added MPEA after 0.5 turn revealed extensive nano-structuring as evident from Fig. 12 (a–c). The average grain size was measured to be 33 ± 19 nm. Clearly, Si addition has significantly enhanced the extent of grain refinement during HPT processing. Further, evidence of a deformation-induced HCP phase was present as indicated by the arrow marked in the SAD pattern. The volume fraction of this HCP phase seemed to be insignificant as suggested by a very faint signature in the diffraction pattern coupled with no peak observed in XRD patterns. Therefore, we focussed on the deformation behavior of FCC phase only. HRTEM images shown in Fig. 12 (d, e) revealed the formation of stacking faults within the nano-structured grains. On increasing the number of HPT turns to 5, the Si-added MPEA showed nano-structuring at both the center and the edge locations. TEM investigations at the center of the 5 turn HPT-processed Si-added MPEA are shown in Fig. 13. Clearly, there is the formation of well-defined grain boundaries at the center of the 5 turn HPT-processed disk. Further, the average grain size was measured to be 46 ± 26 nm. On traversing from center to edge, a remarkable microstructural refinement led to an average grain size of 23 ± 14 nm (Fig. 14 (a–c)). This is one of the finest average grain sizes reported for any FCC metal or alloy subjected to HPT processing. It is interesting to note that the

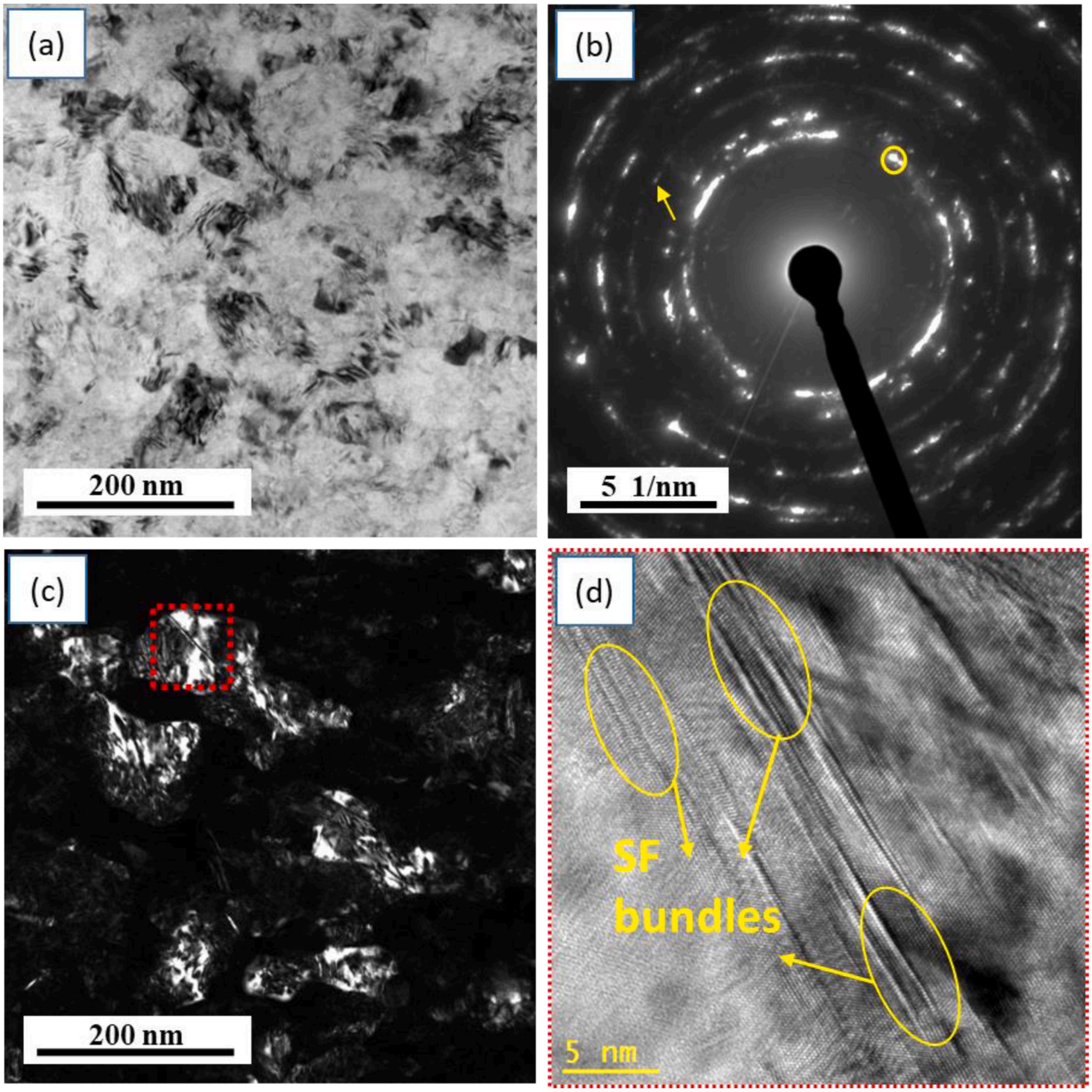

Fig. 10. TEM images of Si-free MPEA at the edge of 5 turns HPT-processed specimen (a) BF TEM image showing appearance of nano-grains, (b) corresponding SAD pattern, (c) DF TEM images produced using the encircled diffraction spot in (b), and (d) HRTEM image of the marked region in (c).

grains with a diameter as low as 15 nm revealed the formation of both bundles of stacking faults and nano-twins as confirmed by HRTEM images shown in Fig. 14 (d, e) and Fig. 14 (f, g), respectively. Notably, despite the formation of the HCP phase at a fairly early stage of HPT processing in both MPEAs, its volume fraction remained insignificant despite an application of a very large shear strain of ~180.

It is worth noting that for most samples investigated in this study the average grain size values determined by TEM are larger than the crystallite size obtained by XLPA and listed in Tables 2 and 3. The only exception is the edge of the Si-added disk processed for 5 turns of HPT where the two size values are close together (23 versus 19 nm). The smaller values of the crystallite size determined by XLPA can be explained by the high sensitivity of XRD on the orientation differences inside the grains. These misorientations break the coherency of X-rays scattered from the grains, thereby resulting in a smaller crystallite size compared to the grain size. Such orientation differences can be caused by dislocation walls or subgrain boundaries. Similar difference between the grain and crystallite sizes has already been observed in all SPD-processed metals and alloys (Gubicza, 2014). A former study showed that when the grain size approaches 20 nm, the grains have no substructure, yielding a practical agreement between the grain and crystallite sizes (Gubicza, 2022). The same was observed for the edge of the Si-added disk processed for 5 turns.

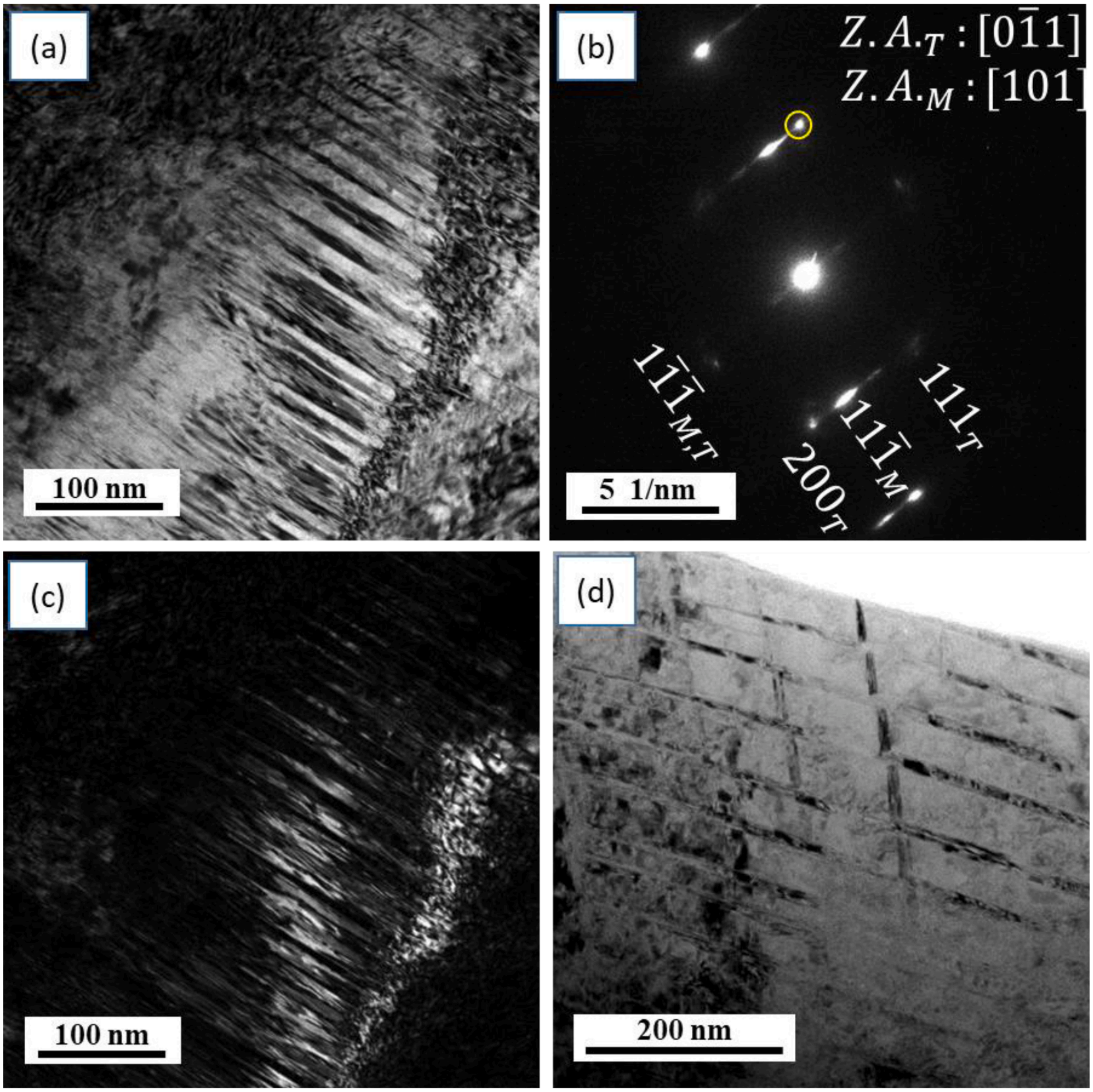

Fig. 11. TEM images of Si-added MPEA at the center of 0.5 turns HPT-processed specimen (a) BF TEM image showing finely spaced nano-twins, (b) corresponding SAD pattern, (c) DF TEM image produced using the encircled diffraction spot in (b), and (d) BF TEM image illustrating twin-twin intersection causing grain sub-division.

4. Discussion

In the present work, the defining role of Si addition (5 atomic % to a non-equiatomic CoCrNiMn MPEA) during HPT is elucidated. Si addition led to several interesting observations, and plausible genesis and implications are discussed below.

4.1. Plasticity mechanisms

In the present study, specimens were subjected to a high pressure of 6 GPa and a shear strain of up to ~180. Many FCC materials with medium to low SFE like austenitic stainless steels (Gubicza et al., 2016), HEAs like $Fe_{40}Mn_{40}Co_{10}Cr_{10}$ (Chandan et al., 2021a), $Fe_{20}Mn_{20}Co_{20}Cr_{26}Ni_{14}$ (Moon et al., 2018) etc. undergo TRIP effect during similar HPT processing parameters. The plasticity mechanisms in the FCC phase are governed by its SFE (Grässel et al., 2000; Madivala et al., 2018), which is strongly dependent on its chemical composition (Gallagher, 1970). In the present case, the addition of Si and removal of Mn resulted in the lowering of the SFE from ~40 to ~20 mJ/m^2. The lower SFE of the Si-added MPEA reflected in an increased fraction of annealing twins in the initial

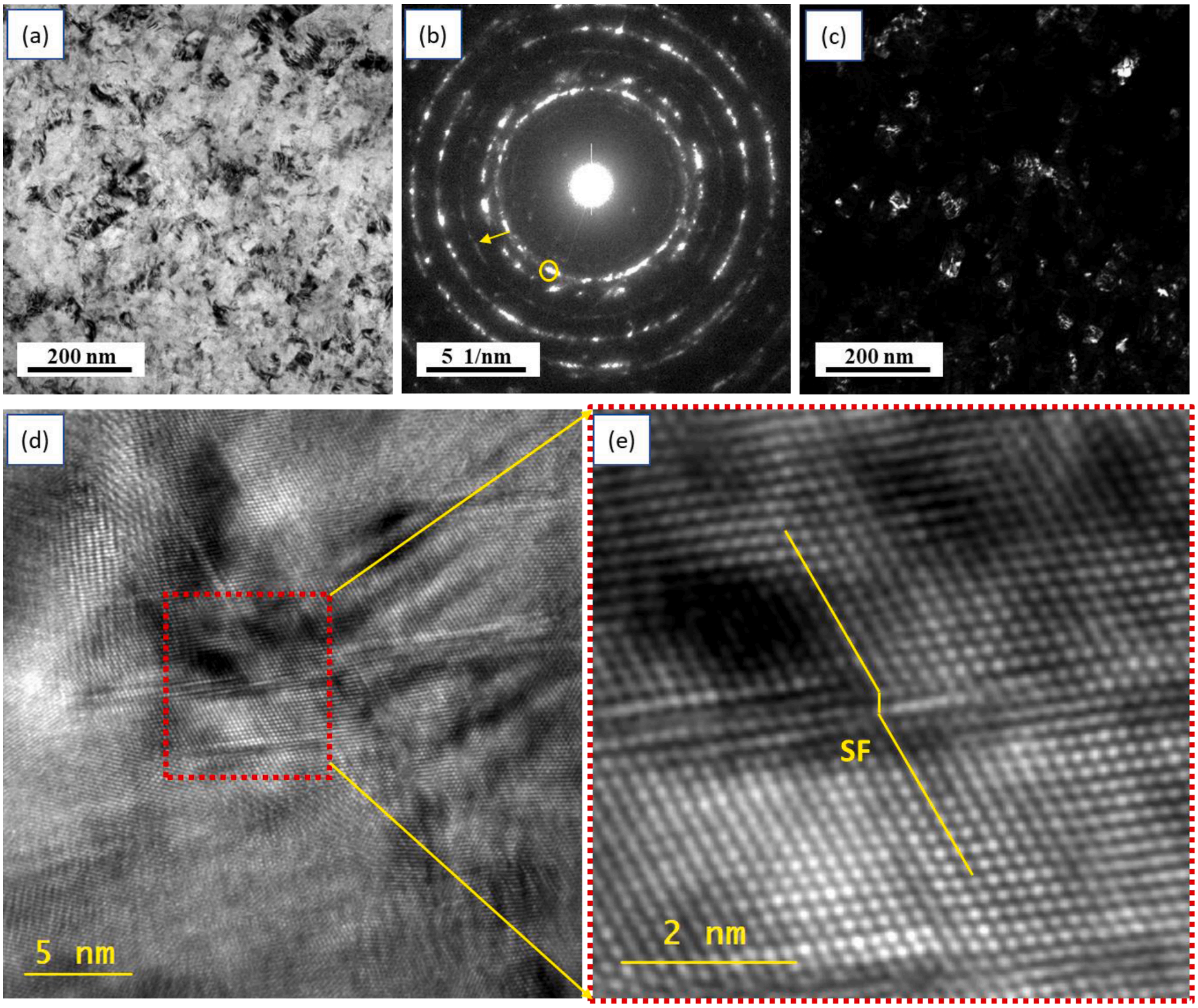

Fig. 12. TEM images of Si-added MPEA at the edge of 0.5 turns HPT-processed specimen (a) BF TEM image showing appearance of nano-grains, (b) corresponding SAD pattern, (c) DF TEM images produced using the encircled diffraction spot in (b), (d) HRTEM image showing occurrence of planar faults, and (e) HRTEM confirming the planar fault to be stacking fault.

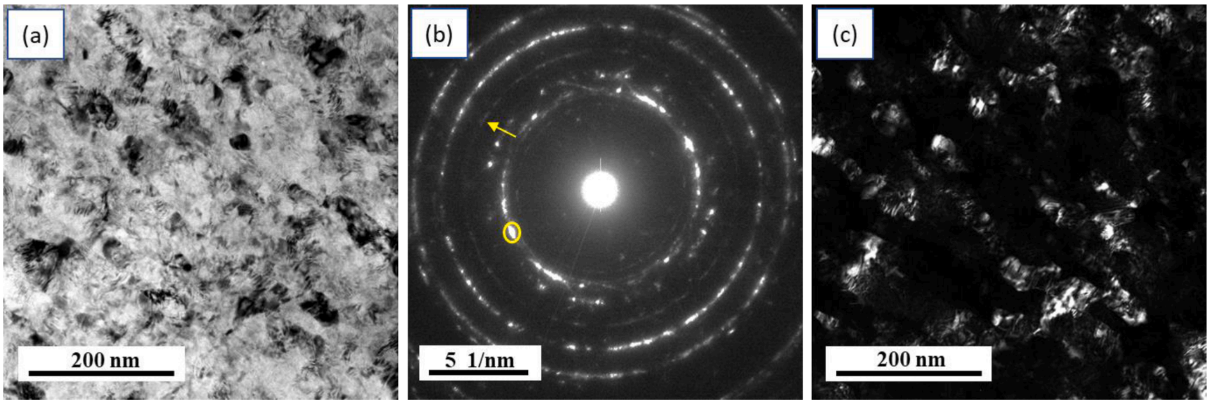

Fig. 13. TEM images of Si-added MPEA at the center of 5 turns HPT-processed specimen (a) BF TEM image showing appearance of nano-grains, (b) corresponding SAD pattern, and (c) DF TEM images produced using the encircled diffraction spot in (b).

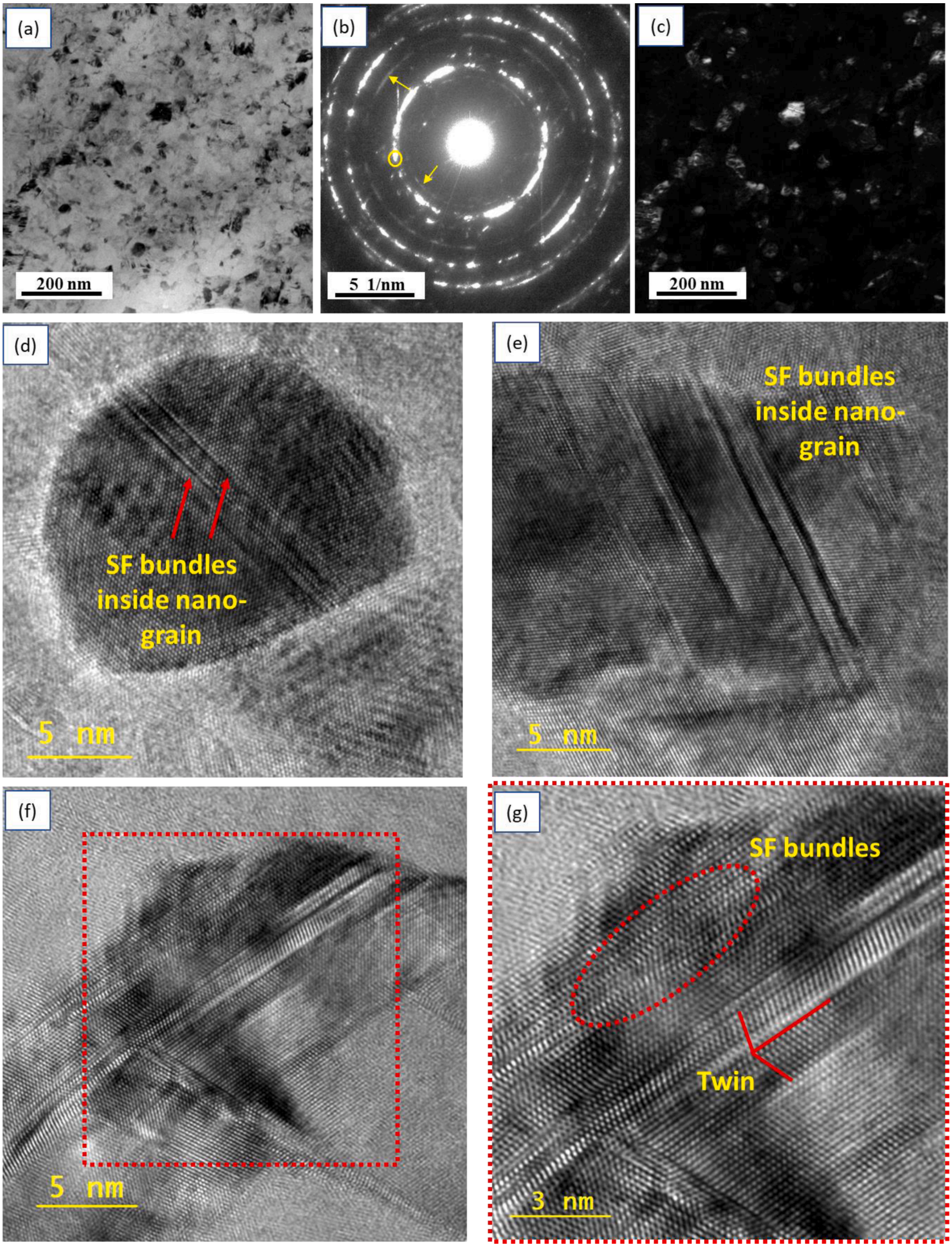

Fig. 14. TEM images of Si-added MPEA at the edge of 5 turns HPT-processed specimen (a) BF TEM image showing extensive nano-structuring, (b) corresponding SAD pattern, (c) DF TEM images produced using the encircled diffraction spot in (b), (d, e) HRTEM image showing the occurrence of planar faults inside a nano-grain, (f) HRTEM image showing intersecting planar faults, and (g) magnified image of the marked region in (f) confirming the formation of twins and stacking faults within the nano-grains.

condition and is in line with the previous research works on the role of Mn and Si on SFE of FCC complex concentrated alloys, austenitic stainless steels, and TWIP steels (Guo et al., 2020; Li and Raabe, 2017; Tian and Zhang, 2009; Das, 2016). Despite these factors, both the studied MPEAs showed limited TRIP effect (insufficient to be revealed by XRD). This confirmed the remarkable mechanical stability of the FCC phase despite being subjected to high pressure and shear strain. Such high stability of the FCC phase is due to the fact that despite the partial substitution of Mn by Si in the CoCrNiMn alloy, the SFE of the Si-added alloy is in the “medium” range where deformation twinning is prominent.

While the addition of Si and the consequent lowering of the SFE did not lead to any perceptible increase in the TRIP effect in the CoCrNiMn MPEA, it certainly resulted in a remarkable rise in the propensity of twinning. This was evident from the 5 times and 1.6 times rise in twin fault probability during early (center of 0.5 turn HPT-processed specimens) and later (edge of 5 turns HPT-processed specimen) stages of HPT processing, respectively, for the Si-added MPEA compared to the Si-free counterpart. In this context, it is worth noting that in earlier works, minor alloying addition or variation in initial grain size affected the plasticity mechanisms and microstructure evolution only during the initial stages of HPT processing. With further increase in strain, a similar saturation state of microstructure was attained. For instance, the addition of boron to Ti-6Al-4 V alloy led to refined initial microstructure and introduced an additional TiB phase, however, during HPT processing, microstructure evolution was different for these two alloys only in the initial stages of deformation (at low shear strains) and subsequently, an identical deformation response was observed for both alloys at higher strains (Roy et al., 2022). Likewise, HPT processing of a V containing FCC HEA with different initial grain sizes led to differences in the deformation mechanisms, especially notable at low and intermediate levels of strain but resulted in microstructures with similar saturation grain size at higher strains (Asghari-Rad et al., 2019). Unlike these reports, Si addition had a sustained implication on the plasticity mechanisms over the entire range of shear strain applied in this study, which is a novel observation. Apart from a significantly higher twin fault probability at both early and later deformation stages, a marked variation in the strain accommodation mechanism inside the nano-grains was noted for the studied alloys. Although an abundance of planar faults inside the nano-grains was observed for both alloys, the Si-free MPEA showed bundles of stacking faults, whereas the Si-added MPEA revealed the formation of nano-twins even inside the grains having a diameter as small as ~15 nm, showing the defining role of Si.

In general, the tendency for twinning increased for both Si-free and Si-added MPEAs with increasing shear strain (see Tables 2 and 3). On one hand, this trend is consistent with the theory which suggests that with increasing shear strain, the stresses are also enhanced in the material, leading to an activation of a greater number of twinning systems. On the other hand, it was also suggested in a former study that with increasing strain, the critical stress necessary for twinning was enhanced due to grain refinement, and at a grain size of about 1 μm this critical stress is higher than the flow stress of CoCrFeMnNi HEA, i.e., twinning hardly occurs in this alloy (Sun et al., 2018). The latter argumentation does not take into account that the stresses inside the material can be higher than the flow stress. For instance, at gliding obstacles, such as Lomer-Cottrell locks or grain boundaries, dislocation pile ups form and the stresses at these locations can be much higher than the flow stress. The stress concentration sites can serve as nuclei of twin formation. With increasing strain, the higher dislocation density and the smaller grain size result in a higher number of twin nucleation sites, therefore a higher probability of twinning is expected in FCC MPEAs. Moreover, a very high pressure (about 6 GPa) is applied during HPT which can also yield high internal stresses in the material. Therefore, even if the critical twinning stress is enhanced with decreasing the grain size, its value can be exceeded by the stresses developed in the HPT-processed samples. In addition, with decreasing grain size to the nanocrystalline regime, the degree of dislocation dissociation increases which also promotes deformation twinning (Zhu et al., 2012).

Apart from deformation via twinning, both Si-free and Si-added alloys revealed a very high dislocation density of the order of 10^{16} m^{-2} in the FCC phase even at the lowest studied strain (at the center of the 0.5 turn HPT-processed specimens), indicating an important role of dislocation slip. Notably, at any HPT processing condition and location of examination, the dislocation density was higher in the Si-added MPEA compared to the Si-free MPEA. It is well-established that the HPT process involves competing phenomena of dislocation generation to accommodate the strain and dynamic recovery mechanisms (Lee et al., 2015). Particularly, at higher shear strains, this competition between the dislocation generation and multiplication with their rearrangement and annihilation results in the attainment of a saturation state of dislocation density. In this context, the saturation value of dislocation density, which is obtained at the edge location of both the alloys only after 0.5 turn of HPT processing is ~30% higher in the Si-added alloy compared to the Si-free alloy. Such an enhanced dislocation density in the Si-added MPEA can result from two different reasons. Firstly, it is attributed to high lattice distortion (δ (Zhang et al., 2008) in Si-added is ~0.019 compared to 0.012 in Si-free MPEA). A highly distorted lattice around the Si atoms can hinder the motion of dislocations during annihilation, thereby resulting in a higher saturation dislocation density (Edalati et al., 2014). Secondly, the reduced SFE in the Si-added MPEA led to (i) a greater propensity of twinning, and twin boundaries also act as obstacles against dislocation motion necessary for annihilation, and (ii) a larger distance between the Shockley partials in dissociated dislocations which would make their recombination more difficult and hence limiting the likelihood of dynamic recovery processes.

On comparing the evolution of dislocation density during HPT processing with the other reported FCC MPEAs exhibiting ~1×10^{16} m^{-2} for $Fe_{35}Mn_5Co_{10}Cr_{15}Ni_{25}V_{10}$ alloy (Asghari-Rad et al., 2019), 1.5×10^{16} m^{-2} for FeCoCrNi alloy (Gubicza et al., 2019), 1.94×10^{16} m^{-2} for CoCrFeMnNi alloy (Gubicza et al., 2019) and 2.36×10^{16} m^{-2} for $Fe_{35}Mn_{35}Co_{10}Cr_{10}Ni_{10}$ alloy (Chandan et al., 2022), the Si-added alloy showed one of the highest saturation values of dislocation density (~3.7×10^{16} m^{-2}) if we take the experimental errors of 10–15% into consideration. The aggravated dislocation density in the Si-added alloy cannot be independently explained based on either lattice distortion or SFE. For instance, $Fe_{35}Mn_5Co_{10}Cr_{15}Ni_{25}V_{10}$ alloy has a remarkably higher lattice distortion (δ) compared to Si-added MPEA, yet the Si-added alloy showed ~3.7 times greater value of the saturation dislocation density (Asghari-Rad et al., 2019). Likewise, the FeCoCrNi alloy has a higher saturation value of twin fault probability (~3%) compared to the Si-added MPEA (~2.4%) alluding to a lower SFE value in the former alloy (Gubicza et al., 2019). Despite this, the Si-added alloy showed ~2.5 times greater saturation value of dislocation density than the FeCoCrNi alloy. This suggests that the saturation value of dislocation density is

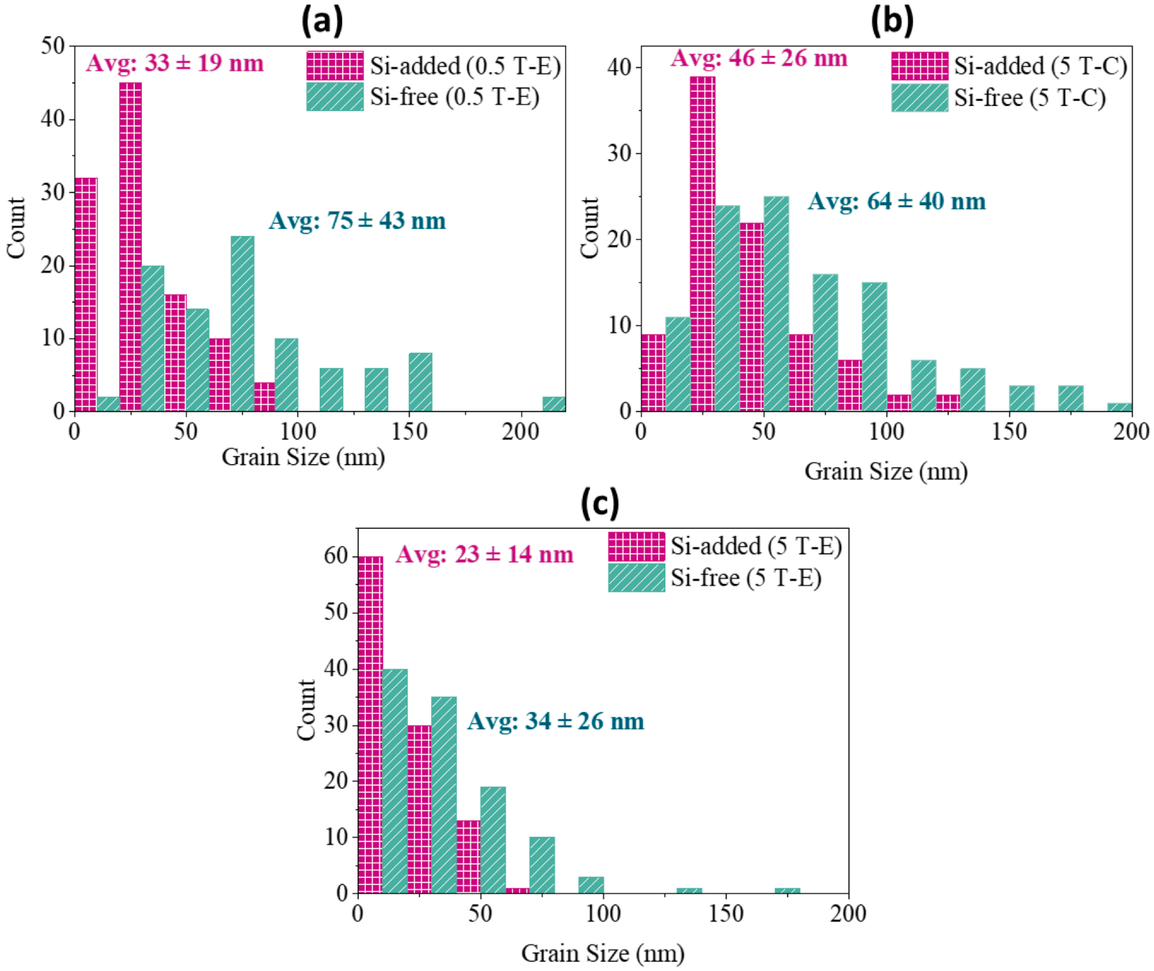

Fig. 15. Comparison of grain size distribution in Si-free and Si-added MPEAs after HPT processing: (a) 0.5 turn at edge location, (b) 5 turns at center location, (c) 5 turns at edge location (Note: average and standard deviations of grain sizes measured using TEM images are provided along with the grain size distribution).

a combined effect of lattice distortion and SFE.

4.2. Mechanisms of grain refinement

For understanding the effect of Si addition on the extent and uniformity of microstructural refinement during HPT processing at a different stage, we plotted the grain size distribution (Fig. 15) based on the values measured from TEM DF micrographs employing the ImageJ software. For all the conditions, a minimum of 100 grains were considered. Si addition ubiquitously resulted in the reduction in the mean grain size after HPT processing. A careful analysis of grain size distribution (Fig. 15) revealed the following key takeaways:

(i) Si addition led to extremely accelerated grain refinement and nano-structuring. The average grain size at the edge location in the Si-free MPEA after 5 turns of HPT processing (~34 nm) was the same as that of the Si-added MPEA after only 0.5 turn of HPT processing (~33 nm). It is worth noting that even the Si-free MPEA shows excellent microstructural refinement in terms of minimum achievable grain size when compared to other FCC MPEAs after similar HPT-processed conditions (Chandan et al., 2022; Asghari-Rad et al., 2019).

(ii) Although the average grain size for the Si-free MPEA was < 100 nm in all the HPT-processed conditions and falls in the category of nano-structured material, there was a large spread in the grain size distribution. In all the conditions, certain grains exceeded even 150 nm, indicating an incomplete nano-structuring in the Si-free alloy. In contrast, the Si-added MPEA could achieve complete nano-structuring at the edge location for the 5 turns of HPT processing.

The genesis of the greater extent and rapid rate of microstructural refinement in the Si-added MPEA can be explained by the difference in the underlying mechanisms of grain refinement in the two alloys as illustrated schematically in Fig. 16. While both Si-free

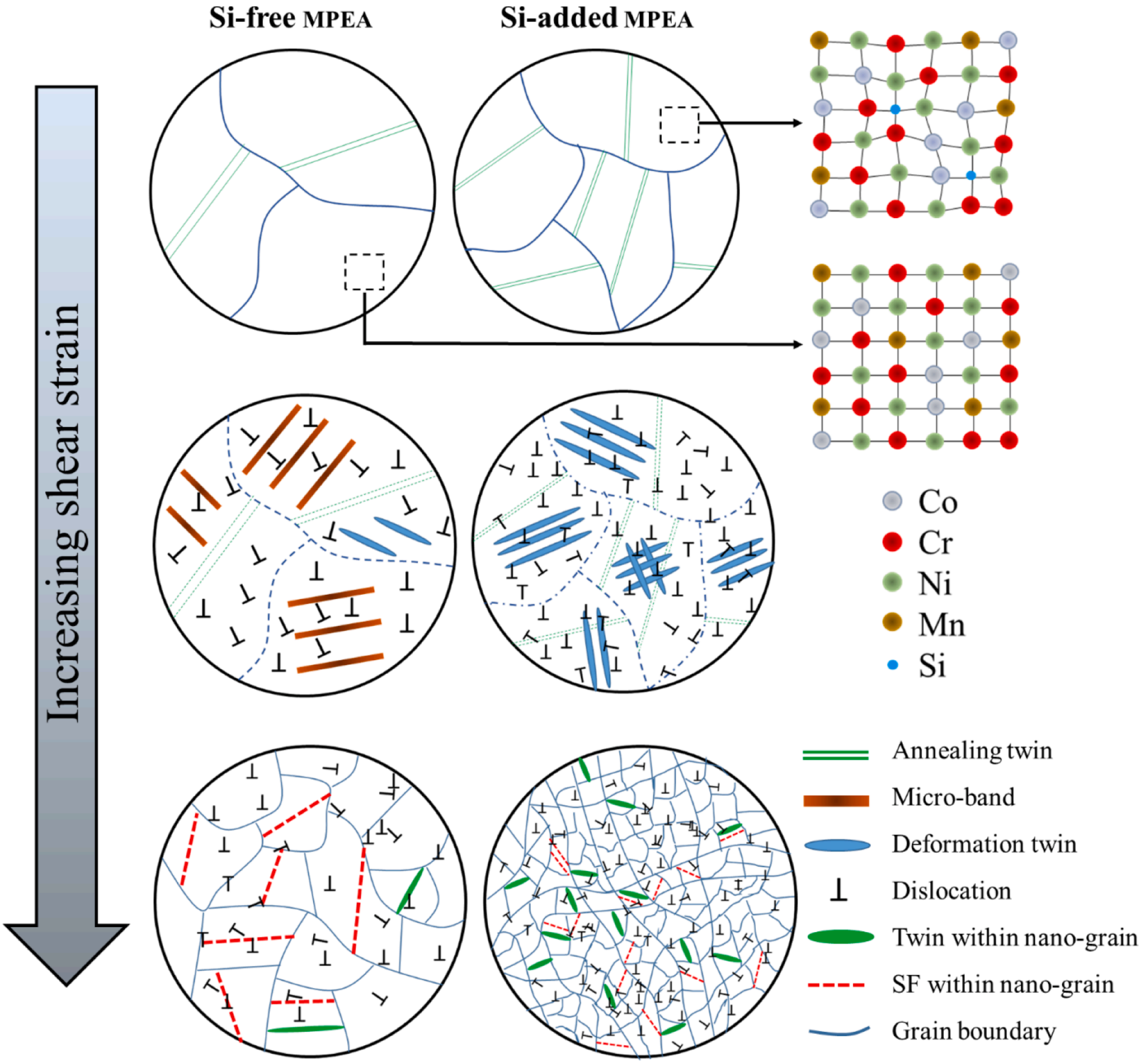

Fig. 16. Schematic representation of the microstructure evolution in Si-free and Si-added MPEAs during HPT processing.

and Si-added MPEAs consisted of a single-phase FCC structure in the initial condition, the Si-added alloy showed slightly finer grain size and a higher fraction of annealing twins compared to the Si-free alloy. While the former is attributed to the solute drag effect caused by the Si atoms, the latter can be attributed to the role of Si addition and Mn reduction in lowering the SFE of the MPEA. Moreover, the addition of smaller Si atoms led to a greater lattice distortion. In the early stage of HPT processing (at the lowest studied strain, that is, at the center of 0.5 turn HPT-processed specimen), the differences in SFE and SSS in the two alloys manifested as largely different deformation features. The mechanism of microstructure sub-division showed a prominent difference in the studied alloys in the initial stage of HPT processing (Fig. 16). The Si-added MPEA was fragmented extensively by the finely spaced nano-twins (~20 nm) and secondary twins compared to a lesser extent of grain sub-division via coarser micro-bands (100–350 nm average spacing) and sporadically occurring deformation twins (~130 nm spacing) in the Si-free MPEA. The significantly greater extent of grain subdivision in the early stage of HPT processing has played a pivotal role in the microstructural refinement of the Si-added MPEA in subsequent HPT processing. The combined effect of greater lattice distortion and a large number of interfaces created by finely spaced deformation twin formation led to significantly higher dislocation density in the Si-added MPEA (discussed in detail in Section 4.1). A higher dislocation density can facilitate the early formation of low-angle grain boundaries (LAGBs) that would eventually transform into high-angle grain boundaries (HAGBs) in order to accommodate the increasing misorientation via dislocation accumulation in the Si-added MPEA during HPT (Wu et al., 2017; Asghari-Rad et al., 2019). Even when nano-structuring was achieved in both alloys, with increasing shear strain the Si-added MPEA showed a remarkable tendency for twinning creating HAGBs within the nanograins. In contrast, Si-free MPEA showed deformation via the creation of stacking faults within the nanograins, which failed to create additional HAGBs.

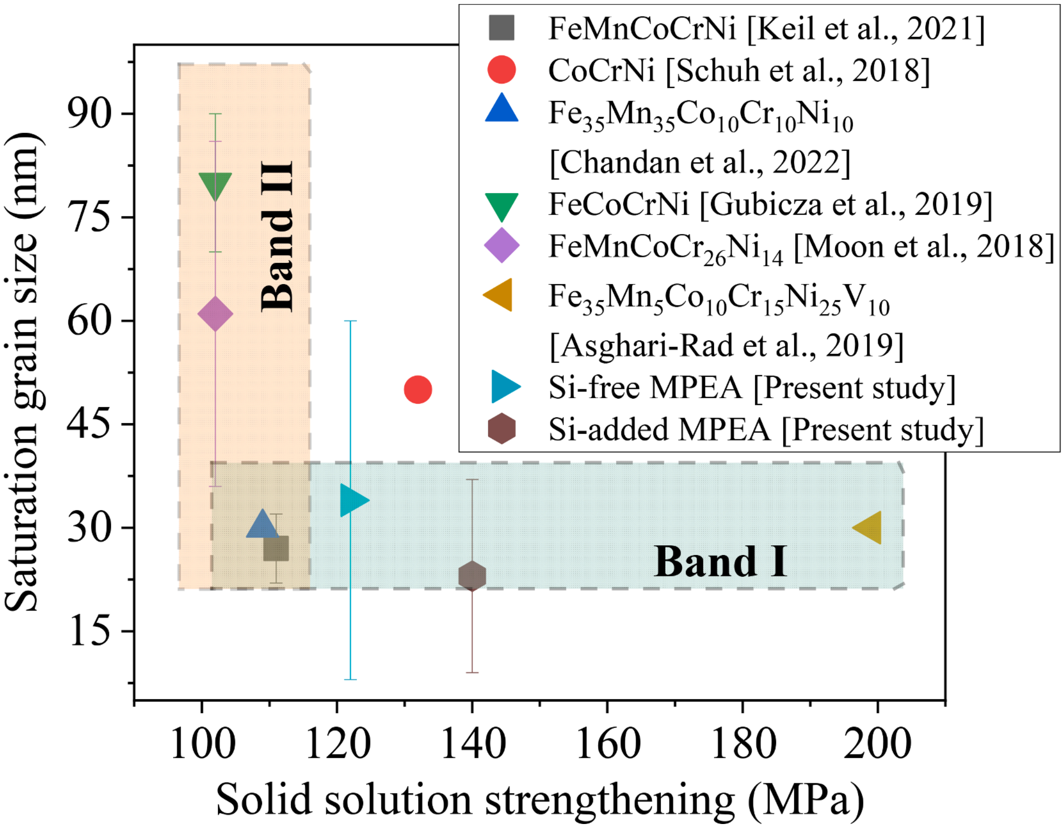

Fig. 17. Variation of finest grain size after HPT processing as a function of solid solution strengthening for different FCC MPEAs.

The present study clearly showcases the important role of SFE in alloys prone to the formation of deformation twins in achieving a higher extent of nano-structuring. This is an apparent contradiction with the report of Edalati et al. (2014) who showed an insignificant role of SFE on the minimum grain size achieved for various binary FCC alloys subjected to HPT processing. The difference between the two observations can be explained by the strongly suppressed recovery and recrystallization in highly alloyed MPEAs. The high density of defects (e.g., dislocations) formed due to the low SFE yields an elevated driving force for recovery and recrystallization, and the higher propensity to these processes inhibits the achievement of very small grain sizes in low-alloy materials. On the other hand, in MPEAs the high alloying effect decreases the probability of the occurrence of recovery and recrystallization, thereby opening the door for the formation of a very fine grain size due to the high density of dislocations and twin faults. Thus, the synergy of the alloying and low SFE effects yielded the extremely low grain size in the Si-added MPEA studied in the present work.

Previous studies in dilute FCC alloys (Edalati et al., 2014) suggested that SSS in FCC metals and alloys dictates the minimum achievable grain size through HPT processing. To investigate the applicability of the same in various FCC MPEAs, we calculated the SSS for different alloys using the Varvenne model (Varvenne et al., 2016) whose detail can be found in Appendix A1. Fig. 17 shows the grain size achieved for different FCC MPEAs during HPT processing as a function of SSS. Clearly, there is no direct correlation between grain refinement after HPT and SSS for FCC MPEAs. For instance, on increasing the SSS contribution from 100 to 200 MPa, there is no proportionate change in the saturation grain size as indicated by the shaded band I in Fig. 17. Further, for a similar range of SSS MPEAs lying in band II showed remarkably different saturation grain size after HPT. Hence, this suggests that SSS alone cannot explain the extent of grain refinement in FCC MPEAs, and there is a need to account for the SFE and the ensuing deformation twinning during HPT to understand the extent and mechanisms of nano-structuring.

4.3. Strengthening mechanisms

Both the Si-free and Si-added MPEAs showed a significant increase in hardness after being subjected to HPT processing. However, the Si-added MPEA showed a faster rate of hardness increase than the Si-free MPEA in the initial stages of HPT processing. For instance, at the center after 0.5 turn by HPT, the average hardness values in the Si-added MPEA and the Si-free MPEA were 439 ± 38 Hv and 348 ± 22 Hv, respectively. It should be noted that the average hardness at the centers was calculated considering the average values from −1 mm to +1 mm on either side of the centers of the discs. This is because the microstructural parameters, especially those obtained

Table 4
Comparison of theoretical and experimentally determined yield strengths in Si-free and Si-added MPEAs after different stages of HPT processing using conventional strengthening contributions. σ_0, σ_{Taylor} and σ_{HP} correspond to the intrinsic lattice strength (or friction stress), the Hall-Petch strengthening due to twin boundaries as twin spacing is finer than grain boundaries and Taylor hardening due to dislocation density, respectively. The sum of these three contributions gives the theoretical yield strength (σ_{YS}^{Th}) which is compared with experimental one (σ_{YS}^{Exp}) obtained from the hardness.

Specimen		σ_0 (MPa)	σ_{Taylor} (MPa)	σ_{HP} (MPa)	Theoretical σ_{YS}^{Th} (MPa)	Experimental σ_{YS}^{Exp} (MPa)	% Difference $\frac{\lvert\sigma_{YS}^{Exp} - \sigma_{YS}^{Th}\rvert}{\sigma_{YS}^{Exp}} * 100$
Si-free MPEA	0.5 C	122	1322	1009	2453	1148	114
	0.5 E	122	1941	2018	4081	1898	115
	5 C	122	2018	2179	4319	1874	130
	5 E	122	2055	2330	4507	2013	124
Si-added MPEA	0.5 C	140	1528	2256	3924	1450	171
	0.5 E	140	2366	2669	5175	2016	157
	5 C	140	2400	2539	5079	1934	163
	5 E	140	2433	2853	5426	2096	159

using XLPA were acquired using a beam of 2 mm length. The higher hardness at the center of the Si-added MPEA after 0.5 HPT turn can be attributed to a greater dislocation density and the higher propensity of twinning. At the edge of 0.5 turn HPT-processed specimens, the average hardness in Si-added MPEA (611 ± 8 Hv) is higher compared to the Si-free MPEA (575 ± 12 Hv). Apart from the higher dislocation density and twinning, the increased hardness is attributed to a significantly finer grain size with a smaller spread in grain size distribution in the Si-added MPEA compared to the edge of the Si-free MPEA specimen after 0.5 turn of HPT processing. After 5 turns of HPT processing, the difference in the hardness between the Si-added and Si-free MPEAs has remarkably reduced compared to 0.5 turn of HPT processing. Despite a significantly higher dislocation density, greater extent of grain refinement and a higher propensity of twinning in the Si-added MPEA compared to the Si-free MPEA, the hardness values at the corresponding locations of the disk after 5 turns of HPT processing was only marginally higher for the Si-added MPEA. This is possibly due to a weaker dependence of yield strength on grain size in nano-structured regime indicating a prevalence of grain boundary-mediated plasticity mechanisms as previously suggested in different studies for conventional alloys (Dangwal et al., 2023). However, the maximum hardness obtained was still 20–25 Hv greater in the case of the Si-added alloy.

To quantify the contribution of various strengthening mechanisms at different stages of HPT in the studied alloys, the following equation was used:

$$\sigma_{YS} = \sigma_0 + \sigma_{HP} + \sigma_{Taylor} \tag{4}$$

where σ_{YS} is the yield strength, and σ_0, σ_{HP} and σ_{Taylor} are the intrinsic lattice strength (or friction stress) including SSS, the Hall-Petch strengthening due to twin boundaries as twin spacing is finer than grain size and the Taylor hardening due to dislocation density, respectively. Herein, we ignored the contribution of any secondary phase strengthening due to the highly localized and limited extent of TRIP effect that is insufficient to be detected by XRD. Further, the yield strength in MPa can be estimated as 3.3 times the average hardness measured in Hv. A similar approach is used in earlier studies on HPT (Heczel et al., 2017). Eq. (4) can be rewritten by expanding the σ_{HP} and σ_{Taylor} terms as:

$$\sigma_{YS} = \sigma_0 + K_{HP}\Big/\sqrt{D} + M\alpha\mu b\sqrt{\rho} \tag{5}$$

where K_{HP} is Hall-Petch constant taken as 265 MPa·μm$^{1/2}$ based on the nearest reported composition, which is an equiatomic CoCrNi alloy (Yoshida et al., 2017), D is the average twin spacing, M is the Taylor factor and its value is 3.06, α is a constant taken as 0.2, μ is the shear modulus, b is the Burgers vector and ρ is the dislocation density. The average twin boundary spacing was calculated from the twin fault probability (β) obtained in percentage by XLPA as (Heczel et al., 2017):

$$D = 100 \cdot d_{111}/\beta, \tag{6}$$

where d_{111} is the lattice spacing for planes {111} (about 0.207 nm for the two studied alloys). The calculated values of μ and b are presented in Appendix A1. The intrinsic lattice strength (σ_0) accounts for the Peierls-Nabarro stress (σ_{PN}) and the contribution from the solid solution strengthening (σ_{SSS}). Peierls-Nabarro stress is usually very low in FCC alloys (Varvenne et al., 2016) and therefore can be neglected during the estimation of the σ_0 and therefore $\sigma_0 \approx \sigma_{SSS}$. The contribution of the SSS was estimated from the model developed by Varvenne et al. (2016) for concentrated alloys and the details of the σ_{SSS} calculation are presented in Appendix A1.

Table 4 presents the contributions of different strengthening mechanisms to σ_{YS}. Based on Eq. (5), in general, the theoretically estimated values (σ_{YS}^{Th}) for both alloys under different HPT processing conditions were at least twice the experimental yield strength (σ_{YS}^{Exp}). It is worth noting that the estimated contribution from the Taylor hardening alone exceeded the experimental yield strength. Furthermore, the estimated contribution from the Hall-Petch strengthening also exceeded the experimentally obtained σ_{YS}^{Exp} in most of

Table 5
Modified strengthening contribution of different mechanisms using best fit approach for the Si-free and the Si-added MPEAs subjected to HPT processing. σ_0, σ_{Taylor} and σ_{HP} correspond to the intrinsic lattice strength (or friction stress), the Hall-Petch strengthening due to twin boundaries as twin spacing is finer than grain boundaries and Taylor hardening due to dislocation density, respectively. The sum of these three contributions gives the theoretical yield strength (σ_{YS}^{Th}) which is compared with experimental one (σ_{YS}^{Exp}) obtained from the hardness.

Specimen		σ_0 (MPa)	σ_{Taylor} (MPa)	σ_{HP} (MPa)	Theoretical σ_{YS}^{Th} (MPa)	Experimental σ_{YS}^{Exp} (MPa)	% Difference $\frac{\lvert\sigma_{YS}^{Exp} - \sigma_{YS}^{Th}\rvert}{\sigma_{YS}^{Exp}} * 100$
Si-free MPEA	0.5 C	122	995	82	1199	1148	4.4
	0.5 E	122	1461	164	1747	1898	7.9
	5 C	122	1518	177	1817	1874	3
	5 E	122	1546	190	1858	2013	7.7
Si-added MPEA	0.5 C	140	1116	184	1440	1450	0.7
	0.5 E	140	1728	217	2085	2016	3.4
	5 C	140	1753	207	2100	1934	8.6
	5 E	140	1777	232	2149	2096	2.5

the cases. Such a discrepancy between the experimental and theoretical values of yield strength in HPT-processed FCC MPEAs has recently been reported by Lu et al. (2021). From Table 4, it is evident that the conventional approach for the yield strength of the nanostructured Si-free and Si-added MPEAs processed by HPT results in an unrealistic overestimation which can be explained by the following reasons:

(i) Reduction in the efficacy of grain boundaries (including twin boundaries) in impeding the motion of dislocations when the grain size becomes <100 nm (Dangwal et al., 2023). In this context, it is previously reported that the classical Hall-Petch relationship does not hold true even for sub-micron grains. It is noted that the value of the Hall-Petch exponent has been shown to decrease from −0.5 to −1 when the grain size decreased below 1 μm if the strength is described only with the Hall-Petch formula, i.e., the dislocation hardening was not taken into account with a separate Taylor term (Chinh et al., 2023). This change is most probably caused by the dislocation strengthening due to the very high dislocation density formed during SPD which yielded an additional enhancement of the strength (Dangwal et al., 2023). On the other hand, for grain size under 100 nm the strength was only slightly enhanced with decreasing the grain size due to enhanced role of grain boundary mediated deformation mechanisms, such as grain boundary sliding, whose occurrence requires a low stress (Gubicza, 2017). Furthermore, for nanostructured materials a modification of the Hall-Petch slope (K_{HP}) to a lower numerical value may also occur which is unknown for many compositions.

(ii) The above calculation relies on α and K_{HP} values that were obtained from previous studies where either the Taylor formula or the Hall-Petch equation was applied individually. However, in the present nanostructured materials processed by HPT, grain boundaries (including twin boundaries) are most probably decorated with substantial fraction of dislocations (both pile up of dislocations at grain boundaries and geometrically necessary dislocations (GNDs)). Such a microstructure wherein grain boundaries are decorated with a high density of dislocations, a gliding dislocation inside the grain would interact directly with dislocations at grain boundary and not the grain boundary itself. Therefore, the strengthening effect of grain boundary dislocations is taken into account in both Taylor and Hall-Petch strengthening, i.e., there is an overlapping effect of the two different contributions. Clearly, the conventional estimation of the strength using an additive approach for Hall-Petch and Taylor-type strengthening contributions, results in accounting for dislocations present at grain boundaries twice.

Because of the complex interplay of grain boundaries and dislocations at grain boundaries, their exact strengthening contribution is difficult to estimate due to the unknown values of α and K_{HP} in the Taylor and Hall-Petch equations, respectively. One way to estimate these variables is to search for the best fit between the estimated and the experimental yield strength values using “Solver” module of MS-Excel, that minimizes the sum of squares of the differences between the theoretical and experimental yield strength values ($\Sigma(\boldsymbol{\sigma}_{YS}^{Th} - \boldsymbol{\sigma}_{YS}^{Exp})^2$). Such an approach was previously employed for CoCrFeMnNi high-entropy alloys processed by HPT (Heczel et al., 2017). This approach yielded α and K_{HP} values of 0.149 and 21.57 MPa·μm$^{1/2}$ for the present nano-structured alloys if both Si-free and Si-added samples are handled together in the analysis. As shown in Table 5, with these values of α and K_{HP}, a much better agreement between the theoretical and experimental yield strength values was achieved for both Si-free and Si-added MPEAs processed using HPT.

It is worth noting that for the present nano-structured materials, both α and K_{HP} are lower than for conventional coarse-grained materials. Namely, α reduced by ~25% whereas K_{HP} reduced by an order of magnitude compared to coarse-grain materials. The significant drop in Hall-Petch constant (K_{HP}) can be attributed at least partly to the overlapping effect of Hall-Petch and Taylor hardening contributions due to the high amount of dislocations accumulated at the grain boundaries, as discussed above. Further, various reports confirm the activation of grain-boundary mediated plasticity mechanisms in nano-structured materials (Gubicza, 2017). The low Hall-Petch slope for metallic materials with obstacle spacing (grain size or twin boundary spacing) smaller than 100 nm has also been shown recently for different metals (Dangwal et al., 2023). In addition, the relatively low value of α can be related at least partly to the high alloying effect in both Si-free and Si-added MPEAs. Namely, the high friction stress and the sluggish diffusion in

MPEAs can hinder the arrangement of dislocations into low energy configurations such as dipoles. Then, the less clustered dislocation structure usually have a lower value of α (Gubicza, 2017) in accordance with the present observation.

The segregation of solute atoms (e.g., Si) at dislocations can also reduce their stress field, thereby weakening the interaction between dislocations and lowering the value of α. This is an indirect effect of alloying on the yield strength beside the direct hardening effect taken into account by the term σ_0 in Eq. (5). The high alloying effect in MPEAs can hinder dislocation annihilation, thereby increasing the dislocation density obtained after HPT which is also an indirect influence of alloying on the yield strength. Thus, the alloying effect can cause a very high dislocation density in MPEAs, however, the Taylor strengthening effect of these dislocations is weaker due to the lower α value. The Hall-Petch strengthening can also be influenced indirectly by the solute atoms. Namely, if they segregated at grain boundaries, it can yield grain boundary relaxation, thereby changing the critical stress necessary for the emission of dislocations from grain boundaries, i.e., the value of K_{HP}.

It is worth noting that an overlapping between the SSS and the Hall-Petch or Taylor strengthening effects may also occur which can explain the overestimation of the total strength when these contributions are simply added. For instance, if a gliding dislocation meet other dislocations decorated with solute atoms (e.g., Si), it interacts with these dislocations and the segregated solutes together; therefore, the separation of the solute atom strengthening and the dislocation hardening is difficult. The situation is similar for the Hall-Petch strengthening effect if solute atoms are accumulated at grain boundaries (including twin boundaries). This may cause an overestimation of the yield strength when the contributions are calculated separately and added linearly. It should also be noted that the validity of the linear addition rule of Taylor and Hall-Petch contributions in the calculation of strength may be a subject of debate even in the latter analysis. Nevertheless, it can be concluded that the conventional equations used for the description of grain boundary and dislocation strengthening cannot be employed for the presently studied MPEAs having deformation-induced nanograins, and at least the modification of the constants used in Taylor and Hall-Petch formulas is necessary.

5. Conclusions

In the present work, HPT-induced plasticity mechanisms and its implications on grain refinement and hardness evolution are studied for Si-free and Si-added non-equiatomic CoCrMnNi MPEAs, having a single-phase FCC structure. The salient findings are enumerated below:

1 The addition of 5 atom% Si at the expense on Mn in a non-equiatomic CoCrMnNi FCC MPEA led to a lowering of the stacking fault energy from ~40 to ~20 mJ/m^{-2}. Despite this lowering of SFE with Si addition, an insignificant TRIP effect was observed in both alloys. However, extensive deformation twinning was triggered in the Si-added alloy in contrast to a low twinning propensity and extensive micro-band formation in the Si-free alloy during early stage of HPT processing. At higher strain levels, notable deformation twinning was observed even for the Si-free alloy, nonetheless, the twin fault probability was still ~50% higher in the Si-added alloy. This is in agreement with the Si-added MPEA having lower SFE compared to the Si-added MPEA but it was still in the medium SFE range so that the TRIP effect was not prominent.

2 Both alloys exhibited a very rapid rise in dislocation density of the order of 10^{16} m^{-2} at the early stage of HPT processing (center of 0.5 turn HPT-processed discs) itself which increased further to reach a saturation value at the edge of 0.5 turn HPT-processed specimen. The dislocation density at any stage was higher in the Si-added MPEA by ~30%, possibly due to greater lattice distortion and higher twin/matrix interface creation owing to lower SFE.

3 Si addition-mediated alteration in plasticity mechanism resulted in accelerated grain refinement, leading to a finer grain size after HPT processing. Accelerated grain refinement is evident from the fact that at the edge location of the disk, Si-added MPEA achieved an average grain size of ~33 nm after only 0.5 turn of HPT processing which could only be achieved after 5 turns of HPT processing for the Si-free MPEA. Further, the saturation grain size at the edge location of the 5 turns of HPT-processed discs was ~23 nm in the Si-added MPEA compared to ~34 nm in case of Si-free MPEA.

4 For FCC MPEAs, both SFE and solid solution strengthening influence the saturation grain size attained after HPT processing, which have been often ignored in previous studies. In the present study, Si-added MPEA showed a finer saturation grain size due to (i) greater lattice distortion that has a pinning effect on defects such as dislocations and grain boundaries, and (ii) the lower SFE resulting in twinning mediated grain sub-division. This work demonstrated the synergistic effect of alloying and low SFE in grain refinement in MPEAs.

5 Si addition had a sustained effect in altering the deformation mechanism even at higher strain during HPT. In addition to the differences in dislocation density, grain size and twin fault probability at the edge location of 5 turn HPT-processed disk, the deformation mechanisms inside the nano-grains were significantly influenced by the Si addition. Nanograins in Si-added MPEA exhibited deformation twinning whereas stacking fault formation was observed for the Si-free MPEA.

6 Si-added MPEA showed a remarkably rapid hardening compared to the Si-free MPEA at early stage of HPT processing. The higher hardness for 0.5 turn HPT-processed disk for Si-added alloy is primarily due to the higher dislocation density leading to a greater Taylor hardening, finer grain size leading to an enhanced Hall-Petch strengthening and greater extent of twinning since twin boundaries are also effective obstacles against dislocation glide. The conventional equations used for the description of grain boundary and dislocation strengthening cannot be employed for the presently studied nanostructured MPEAs, and at least the constants used in Taylor and Hall-Petch formulas should be modified in order to obtain a reasonable agreement between the measured and calculated strength values.

CRediT authorship contribution statement

Kaushal Kishore: Conceptualization, Investigation, Formal analysis, Data curation, Visualization, Writing – original draft, Writing – review & editing. **Avanish Kumar Chandan:** Conceptualization, Investigation, Formal analysis, Data curation, Visualization, Funding acquisition, Writing – original draft, Writing – review & editing. **Pham Tran Hung:** Investigation, Data curation. **Saurabh Kumar:** Investigation, Data curation. **Manish Ranjan:** Investigation, Data curation. **Megumi Kawasaki:** Investigation, Formal analysis, Visualization, Funding acquisition, Writing – review & editing. **Jenő Gubicza:** Conceptualization, Visualization, Supervision, Funding acquisition, Writing – review & editing.

Declaration of Competing Interest

The authors declare that they have no known competing financial interests or personal relationships that could have appeared to influence the work reported in this paper.

Data availability

Data will be made available on request.

Acknowledgement

Fund and a part of equipment support required for carrying out the present study was facilitated by CSIR-National Metallurgical Laboratory, Jamshedpur, India, under the *i*-PSG initiative; Project number: OLP 0346 (A.K.C.). The study was also supported in part by the National Science Foundation of the United States under Grant No. CMMI-2051205 (M.K.). The author AKC would like to acknowledge Dr. Avijit Metya for helping in estimation of the ultrasonic wave velocities for the calculation of shear modulus and Poisson's ratio.

Appendix

A1. Calculation of solid solution strengthening

For estimation of the solid solution strengthening contribution in the studied MPEAs, we applied the analytical model proposed by Varvenne et al. (2016) which provides a formalism to quantify the increase in shear stress at temperature T (in K) and $\dot{\varepsilon}$ the strain rate of deformation, i.e., the solid solution strengthening ($\tau_y(T,\dot{\varepsilon})$) given as:

$$\tau_y(T,\dot{\varepsilon}) = \tau_{yo}\exp\left[-\frac{1}{0.51}\frac{kT}{\Delta E_b}\ln\left(\frac{\dot{\varepsilon}_o}{\dot{\varepsilon}}\right)\right] \tag{A1}$$

where k is the Boltzmann constant, $\dot{\varepsilon}_o$ is a reference strain-rate (Varvenne et al., 2016), τ_{yo} is the shear strength at 0 K and is given as (Varvenne et al., 2016):

$$\tau_{yo} = 0.03589 * \mu * \left(\frac{1+\upsilon}{1-\upsilon}\right)^{\frac{4}{3}} * \left(\sum_n \frac{C_n \Delta\overline{V}_n^2}{b^6}\right)^{2/3} \tag{A2}$$

where μ is shear modulus and υ is the Poisson's ratio, both were determined employing an ultrasonic based non-destructive technique (Hu and Wang, 2016). ΔE_b corresponds to the total energy barrier, i.e., the energy cost of moving a dislocation from energetically favorable to unfavorable potential energy fluctuation over a distance w_c and is given as (Varvenne et al., 2016):

$$\Delta E_b = 0.7767 * \mu * b^3 * \left(\frac{1+\upsilon}{1-\upsilon}\right)^{\frac{2}{3}} * \left(\sum_n \frac{C_n \Delta\overline{V}_n^2}{b^6}\right)^{1/3} \tag{A3}$$

$\Delta\overline{V}_n = V_n - \overline{V}$ is the average misfit volume of element n in the alloy; $\overline{V} = \sum_n C_n V_n$; V_n is the individual atomic volume for element n. The values of the individual volumes V_n for Ni, Co, Cr and Mn was taken as 10.94, 11.12, 12.27 and 12.60 A^3, respectively (Varvenne et al., 2016). V_n for Si was calculated to be 10.23 A^3 from the formalism provided in (Varvenne et al., 2016) and using the lattice parameter of the Ni-Si solid solution taken from Nash and Nash (1987). b is the Burgers vector of full dislocations, and b was obtained as $a/\sqrt{2}$ where a is the lattice parameter obtained from the Nelson-Riley plot (Nelson and Riley, 1945). The calculated values of the shear modulus, Poisson's ratio and Burgers vector are provided in Table A1. The values of the solid solution strengthening were obtained from the above formalism at 300 K as 122 MPa and 140 MPa in the Si-free and Si-added MPEAs, respectively.

Table A1
Calculated values of shear modulus (μ), Poisson's ratio (ν) and magnitude of Burgers vector (b) of the Si-free and Si-added MPEAs.

Parameters	Values
$\mu_{Si\text{-}free}$ (GPa)	79
$\mu_{Si\text{-}added}$ (GPa)	82
$\nu_{Si\text{-}free}$	0.27
$\nu_{Si\text{-}added}$	0.28
$b_{Si\text{-}free}$ (Ȧ)	2.533
$b_{Si\text{-}added}$ (Ȧ)	2.524

A2. Estimation of actual partial dislocation spacing

Position of the intensity peak of Shockley partial dislocations obtained via the WBDF imaging technique is influenced by the dislocation depth within the foil, foil thickness and excitation error (Cockayne, 1972; Cockayne and Vitek, 1974) and therefore correction has to be applied to obtain the actual dislocation width (d_{act}) as (Cockayne, 1972):

$$d_{act} = \sqrt{d_{obs}^2 - \frac{4}{ab}} + \frac{b-a}{ab}, \tag{A4}$$

where

$$a = -\frac{2\pi s_g}{g.\left(b_{p1} + \frac{b_{p1,e}}{2(1-\nu)}\right)} \tag{A5}$$

and

$$b = -\frac{2\pi s_g}{g.\left(b_{p2} + \frac{b_{p2,e}}{2(1-\nu)}\right)}. \tag{A6}$$

d_{obs} is the observed spacing between the partials, b_{pi} is the Burgers vector of ith partial dislocation and $b_{pi,e}$ is its edge component. ν is the Poisson's ratio (see Table A1). s_g is the deviation parameter for the applied $g(3g)$ diffraction condition which is given as (Williams and Carter, 2009):

$$s_g = \frac{1}{2}(n-1)\ |g|^2\ \lambda, \tag{A7}$$

where $n = 3$ for the $g(3g)$ condition and λ is the electron wavelength.

References

An, F., Hou, J., Liu, J., Qian, B., Lu, W., 2023. Deformable κ phase induced deformation twins in a CoNiV medium entropy alloy. Int. J. Plast. 160, 103509. http://doi.org/10.1016/j.ijplas.2022.103509.

Aerts, E., Delavignette, P., Siems, R., Amelinckx, S., 1962. Stacking fault energy in silicon. J. Appl. Phys. 33, 3078–3080. https://doi.org/10.1063/1.1728570.

Asghari-Rad, P., Sathiyamoorthi, P., Bae, J.W., Shahmir, H., Zargaan, A., Kim, H.S., 2019. Effect of initial grain size on deformation mechanism during high-pressure torsion in V10Cr15Mn5Fe35Co10Ni25 high-entropy alloy. Adv. Eng. Mater. 1900587, 1–9. https://doi.org/10.1002/adem.201900587.

Bruder, E., Braun, V., Rehman, H., Marceau, R.K.W., Taylor, A.S., Pippan, R., Durst, K., 2018. Influence of solute effects on the saturation grain size and rate sensitivity in Cu-X alloys. Scr. Mater. 144, 5–8. https://doi.org/10.1016/j.scriptamat.2017.09.031.

Cantor, B., Chang, I.T.H., Knight, P., Vincent, A.J.B., 2004. Microstructural development in equiatomic multicomponent alloys. Mater. Sci. Eng. A 375–377, 213–218. https://doi.org/10.1016/j.msea.2003.10.257.

Chandan, A.K., Hung, P.T., Kishore, K., Kawasaki, M., Chakraborty, J., Gubicza, J., 2021a. On prominent TRIP effect and non-basal slip in a TWIP high entropy alloy during high-pressure torsion processing. Mater. Charact. 178, 111284 https://doi.org/10.1016/j.matchar.2021.111284.

Chandan, A.K., Kishore, K., Hung, P.T., Ghosh, M., Chowdhury, S.G., Kawasaki, M., Gubicza, J., 2022. Effect of nickel addition on enhancing nano-structuring and suppressing TRIP effect in Fe40Mn40Co10Cr10 high entropy alloy during high-pressure torsion. Int. J. Plast. 150, 103193 https://doi.org/10.1016/j.ijplas.2021.103193.

Chandan, A.K., Tripathy, S., Sen, B., Ghosh, M., Chowdhury, S.G., 2021b. Temperature dependent deformation behavior and stacking fault energy of Fe40Mn40Co10Cr10 alloy. Scr. Mater. 199, 113891 https://doi.org/10.1016/j.scriptamat.2021.113891.

Chang, H., Zhang, T.W., Ma, S.G., Zhao, D., Xiong, R.L., Wang, T., Li, Z.Q., Wang, Z.H., 2021. Novel Si-added CrCoNi medium entropy alloys achieving the breakthrough of strength-ductility trade-off. Mater. Des. 197, 109202. http://doi.org/10.1016/j.matdes.2020.109202.

Chinh, N.Q., Olasz, D., Ahmed, A.Q., Safran, G., Lendvai, J., Langdon, T.G., 2023. Modification of the Hall-Petch relationship for submicron-grained fcc metals. Mater. Sci. Eng. A 862, 144419. https://doi.org/10.1016/j.msea.2022.144419.

Cockayne, D.J.H., 1972. A theoretical analysis of the weak-beam method of electron microscopy. Z. Naturforschung 27 a, 452–460. https://doi.org/10.1515/zna-1972-0313.

Cockayne, D.J.H., Vitek, V., 1974. Effect of core structure on the determination of the stacking-fault energy in close-packed metals. Phys. Status Solidi 65 (2), 751–764. https://doi.org/10.1002/pssb.2220650236.

Dangwal, S., Edalati, K., Valiev, R.Z., Langdon, T.G., 2023. Breaks in the Hall-Petch relationships after severe plastic deformation of magnesium, aluminum, copper, and iron. Crystals 13, 413. https://doi.org/10.3390/cryst13030413.

Das, A., 2016. Revisiting stacking fault energy of steels. Metall. Mater. Trans. A 47, 748–768. https://doi.org/10.1007/s11661-015-3266-9.X.

Ding, Z.Y., He, Q.F., Wang, Q., Yang, Y., 2018. Superb strength and high plasticity in laves phase rich eutectic medium-entropy-alloy nanocomposites. Int. J. Plast. 106, 57–72. https://doi.org/10.1016/j.ijplas.2018.03.001.

Edalati, K., Akama, D., Nishio, A., Lee, S., Yonenaga, Y., Cubero-Sesin, J.M., Horita, Z., 2014. Influence of dislocation-solute atom interactions and stacking fault energy on grain size of single-phase alloys after severe plastic deformation using high-pressure torsion. Acta Mater. 69, 68–77. https://doi.org/10.1016/j.actamat.2014.01.036.

Edalati, K., Bachmaier, A., Beloshenko, V.A., Beygelzimer, Y., Blank, V.D., Botta, W.J., Bryła, K., Čížek, J., Divinski, S., Enikeev, N.A., Estrin, Y., Faraji, G., Figueiredo, R.B., Fuji, M., Furuta, T., Grosdidier, T., Gubicza, J., Hohenwarter, A., Horita, Z., Huot, J., Ikoma, Y., Janeček, M., Kawasaki, M., Král, P., Kuramoto, S., Langdon, T.G., Leiv, D.R., Levita, V.I., Mazilkin, A., Mito, M., Miyamoto, H., Nishizaki, T., Pippan, R., Popov, V.V., Popova, E.N., Purcek, G., Renk, O., Révész, Á., Sauvage, X., Sklenicka, V., Skrotzki, W., Straumal, B.B., Suwas, S., Toth, L.S., Tsuji, N., Valiev, R.Z., Wilde, G., Zehetbauer, M.J., Zhu, X., 2022a. Nanomaterials by severe plastic deformation: review of historical developments and recent advances. Mater. Res. Lett. 10, 163–256. https://doi.org/10.1080/21663831.2022.2029779.

Edalati, K., Wang, Q., Enikeev, N.A., Peters, L., Zehetbauer, M.J., Schafler, E., 2022b. Significance of strain rate in severe plastic deformation on steady-state microstructure and strength. Mater. Sci. Eng. A 859, 144231. https://doi.org/10.1016/j.msea.2022.144231.

Estrin, Y., Molotnikov, A., Davies, C.H.J., Lapovok, R., 2008. Strain gradient plasticity modelling of high-pressure torsion. J. Mech. Phys. Solids 56, 1186–1202. https://doi.org/10.1016/j.jmps.2007.10.004.

Filho, F.D.C.G., Ritchie, R.O., Meyers, M.A., Monteiro, S.N., 2022. Cantor-derived medium-entropy alloys: bridging the gap between traditional metallic and high-entropy alloys. J. Mater. Res. Technol. 17, 1868–1895. https://doi.org/10.1016/j.jmrt.2022.01.118.

Gallagher, P.C.J., 1970. The influence of alloying, temperature, and related effects on the stacking fault energy. Met. Trans. 1, 2429–2661. https://doi.org/10.1007/BF03038370.

Grässel, O., Krüger, L., Frommeyer, G., 2000. High strength Fe-Mn-(Al, Si) TRIP/TWIP steels development - properties – application. Int. J. Plast. 16, 1391–1409. https://doi.org/10.1016/S0749-6419(00)00015-2.

Gubicza, J., 2017. Defect Structure and Properties of Nanomaterials. Woodhead Publishing, Duxford, UK.

Gubicza, J., 2014. X-Ray Line Profile Analysis in Materials Science. IGI Global, Hershey, USA.

Gubicza, J., 2022. Reliability and interpretation of the microstructural parameters determined by X-ray line profile analysis for nanostructured materials. Eur. Phys. J. Spec. Top. 231, 4153–4165. https://doi.org/10.1140/epjs/s11734-022-00572-z.

Gubicza, J., El-Tahawy, M., Huang, Y., Choi, H., Choe, H., Labar, J.L., Langdon, T.G., 2016. Microstructure, phase composition and hardness evolution in 316 L stainless steel processed by high-pressure torsion. Mater. Sci. Eng. A 657, 215–223. https://doi.org/10.1016/j.msea.2016.01.057.

Gubicza, J., Hung, P.T., Kawasaki, M., Han, J., Zhao, Y., Xue, Y., Labar, J.L., 2019. Influence of severe plastic deformation on the microstructure and hardness of a CoCrFeNi high-entropy alloy: a comparison with CoCrFeNiMn. Mater. Charact. 154, 304–314. http://doi.org/10.1016/j.matchar.2019.06.015.

Guo, W., Jing, S., Wenjun, L., Liebscher, C.H., Kirchlechner, C., Ikeda, Y., Körmann, F., Xuan, L., Yunfei, X., Dehm, G., 2020. Dislocation-induced breakthrough of strength and ductility trade-off in a non-equiatomic high-entropy alloy. Acta Mater. 185, 45–54. https://doi.org/10.1016/j.actamat.2019.11.055.

Han, L., Rao, Z., Filho, I.R.S., Maccari, F., Wei, Y., Wu, G., Ahmadian, A., Zhou, X., Gutfleisch, O., Ponge, D., Raabe, D., Li, Z., 2021. Ultrastrong and ductile soft magnetic high-entropy alloys via coherent ordered nanoprecipitates. Adv. Mater. 33, 2102139 https://doi.org/10.1002/adma.202102139.

Heczel, A., Kawasaki, M., Labar, J.L., Jang, J., Langdon, T.G., Gubicza, J., 2017. Defect structure and hardness in nanocrystalline CoCrFeMnNi high-entropy alloy processed by high-pressure torsion. J. Alloy. Compd. 711, 143–154. https://doi.org/10.1016/j.jallcom.2017.03.352.

Hirth, J.P., Lothe, J., 1982. Theory of Dislocations. Wiley, New York.

Hohenwarter, A., Pippan, R., 2019. Sample size and strain-rate-sensitivity effects on the homogeneity of high-pressure torsion deformed disks. Metall. Mater. Trans. A 50, 601–608. https://doi.org/10.1007/s11661-018-4989-1.

Hu, E., Wang, W., 2016. The elastic constants measurement of metal alloy by using ultrasonic nondestructive method at different temperature. Math. Prob. Engg. 2016, 6762076 https://doi.org/10.1155/2016/6762076.

Huang, Y., Al-Zubaydi, A., Kawasaki, M., Langdon, T.G., 2014. An overview of flow patterns development on disc lower surfaces when processing by high-pressure. J. Mater. Res Technol. 3, 303–310. https://doi.org/10.1016/j.jmrt.2014.06.005.

Jamalian, M., Hamid, M., Vincentis, N.D., Buck, Q., Field, D.P., Zbib, H.M., 2019. Creation of heterogeneous microstructures in copper using high-pressure torsion to enhance mechanical properties. Mater. Sci. Eng. A 756, 142–148. https://doi.org/10.1016/j.msea.2019.04.024.

Jiang, K., Zhang, Q., Li, J., Li, X., Zhao, F., Hou, B., Suo, T., 2022. Abnormal hardening and amorphization in an FCC high entropy alloy under extreme uniaxial tension. Int. J. Plast. 159, 103463 https://doi.org/10.1016/j.ijplas.2022.103463.

Kawasaki, M., 2014. Different models of hardness evolution in ultrafine-grained materials processed by high-pressure torsion. J. Mater. Sci. 49, 18–34. https://doi.org/10.1007/s10853-013-7687-9.

Kawasaki, M., Figueiredo, R.B., Langdon, T.G., 2011. An investigation of hardness homogeneity throughout disks processed by high-pressure torsion. Acta Mater. 59, 308–316. https://doi.org/10.1016/j.actamat.2010.09.034.

Keil, T., Bruder, E., Brocq, M.L., Durst, K., 2021. From diluted solid solutions to high entropy alloys: saturation grain size and mechanical properties after high pressure torsion. Scr. Mater. 192, 43–48. http://doi.org/10.1016/j.scriptamat.2020.09.046.

Kishore, K., Chandan, A.K., Hung, P.T., Kumar, S., Kawasaki, M., Gubicza, J., 2022. On the enhanced hardening ability and plasticity mechanisms in a novel Mn-added CoCrNi medium entropy alloy during high-pressure torsion. J. Alloy. Compd. 904, 163941 https://doi.org/10.1016/j.jallcom.2022.163941.

Laplanche, G., Kostka, A., Reinhart, C., Hunfeld, J., Eggeler, G., George, E.P., 2017. Reasons for the superior mechanical properties of medium-entropy CrCoNi compared to high-entropy CrMnFeCoNi. Acta Mater. 128, 292–303. https://doi.org/10.1016/j.actamat.2017.02.036.

Lee, D.H., Choi, I.C., Seok, M.Y., He, J., Lu, Z., Suh, J.Y., Kawasaki, M., Langdon, T.G., Jang, J., 2015. Nanomechanical behavior and structural stability of a nanocrystalline CoCrFeNiMn high-entropy alloy processed by high-pressure torsion. J. Mater. Res. 30, 2804–2815. http://doi:10.1557/jmr.2015.239.

Liu, D., Yu, Q., Kabra, S., Jiang, M., Forna-Kreutzer, P., Zhang, R., Payne, M., Walsh, F., Gludovatz, B., Asta, M., Minor, A.M., George, E.P., Ritchie, R.O., 2022a. Exceptional fracture toughness of CrCoNi-based medium- and high-entropy alloys at 20 kelvin. Science 378, 978–983. https://www.science.org/doi/10.1126/science.abp8070.

Liu, S., Lin, W., Zhao, Y., Chen, D., Yeli, G., He, F., Zhao, S., Kai, J., 2020. Effect of silicon addition on the microstructures, mechanical properties and helium irradiation resistance of NiCoCr-based medium-entropy alloys. J. Alloy. Compd. 844, 156162 https://doi.org/10.1016/j.jallcom.2020.156162.

Liu, S.Y., Wang, H., Zhang, J.Y., Zhang, H., Xue, H., Liu, G., Sun, J., 2022b. Trifunctional Laves precipitates enabling dual-hierarchical FeCrAl alloys ultra-strong and ductile. Int. J. Plast. 159, 103438 https://doi.org/10.1016/j.ijplas.2022.103438.

Liu, X., Ding, H., Huang, Y., Bai, X., Zhang, Q., Zhang, H., Langdon, T.G., Cui, J., 2021. Evidence for a phase transition in an AlCrFe2Ni2 high entropy alloy processed by high-pressure torsion. J. Alloy. Compd. 867, 159063. http://doi.org/10.1016/j.jallcom.2021.159063.

Li, Z., Chen, L., Fu, P., Su, H., Dai, P., 2022. The effect of Si addition on the heterogeneous grain structure and mechanical properties of CrCoNi medium entropy alloy. Mater. Sci. Eng. A 852, 143655. https://doi.org/10.1016/j.msea.2022.143655.

Li, Z., Pradeep, K.G., Deng, Y., Deng, Y., Raabe, D., Tasan, C.C., 2016. Metastable high-entropy dual-phase alloys overcome the strength – ductility trade-off. Nature 534, 227–230. https://doi.org/10.1038/nature17981.

Li, Z., Raabe, D., 2017. Strong and ductile non-equiatomic high-entropy alloys: design, processing, microstructure, and mechanical properties. JOM 69, 2099–2106. https://doi.org/10.1007/s11837-017-2540-2.

Luo, H., Sohn, S.S., Lu, W., Li, L., Li, X., Soundararajan, C.K., Krieger, W., Li, Z., Raabe, D., 2020. A strong and ductile medium-entropy alloy resists hydrogen embrittlement and corrosion. Nat. Commun. 11, 3081. https://doi.org/10.1038/s41467-020-16791-8.

Lu, Y., Mazilkin, A., Boll, T., Stepanov, N., Zherebtzov, S., Salishchev, G., Odor, E., Ungar, T., Lavernia, E., Hahn, H., Ivanisenko, Y., 2021. Influence of carbon on the mechanical behavior and microstructure evolution of CoCrFeMnNi processed by high pressure torsion. Materialia 16, 101059. https://doi.org/10.1016/j.mtla.2021.101059.

Madivala, M., Schwedt, A., Wong, S.L., Roters, F., Prahl, W., Bleck, W., 2018. Temperature dependent strain hardening and fracture behavior of TWIP steel. Int. J. Plast. 104, 80–103. https://doi.org/10.1016/j.ijplas.2018.02.001.

Ming, K., Bi, X., Wang, J., 2019. Strength and ductility of CrFeCoNiMo alloy with hierarchical microstructures. Int. J. Plast. 113, 255–268. https://doi.org/10.1016/j.ijplas.2018.10.005.

Miracle, D.B., Senkov, O.N., 2017. A critical review of high entropy alloys and related concepts. Acta Mater. 122, 448–511. https://doi.org/10.1016/j.actamat.2016.08.081.

Mohamed, F.A., Dheda, S.S., 2012. On the minimum grain size obtainable by high-pressure torsion. Mater. Sci. Eng. A 558, 59–63. https://doi.org/10.1016/j.msea.2012.07.066.

Moon, J., Tababchnikova, Y., Qi, E., Estrin, Y., Choi, W., Joo, S., Lee, B., Podolskiy, A., Tikhonovsky, M., Kim, H.S., 2018. Microstructure and mechanical properties of high-entropy alloy Co20Cr26Fe20Mn20Ni14 processed by high-pressure torsion at 77 K and 300 K. Sci. Rep. 8, 11074. https://doi.org/10.1038/s41598-018-29446-y.

Nash, P., Nash, A., 1987. The Ni-Si (Nickel-Silicon) System. Bull. Alloy Phase Diagr. 8, 6–14. https://doi.org/10.1007/BF02868885.

Nelson, J.B., Riley, D.P., 1945. An experimental investigation of extrapolation methods in the derivation of accurate unit-cell dimensions of crystals. Proc. Phys. Soc. 57 (3), 160 (1926-1948).

Nguyen, N.T.C., Asghari-Rad, P., Sathiyamoorthi, P., Zargaran, A., Lee, C.S., Kim, H.S., 2020. Ultrahigh high-strain-rate superplasticity in a nanostructured high-entropy alloy. Nat. Commun. 11, 2736. https://doi.org/10.1038/s41467-020-16601-1.

Paul, A., Liu, X., Kawasaki, M., Liss, K.D., 2023. Inverted magnetic response in severe plastically deformed nanostructured high-entropy alloy. Appl. Phys. Lett. 122, 052402 https://doi.org/10.1016/5.0138040.

Pippan, R., Scheriau, S., Taylor, A., Hafok, M., Hohenwarter, A., Bachmaier, A., 2010. Saturation of fragmentation during severe plastic deformation. Annu. Rev. Mater. Res. 40, 319–343. http://doi.org/10.1146/annurev-matsci-070909-104445.

Renk, O., Hohenwarter, A., Gammer, C., Eckert, J., Pippan, R., 2022. Achieving 1 GPa fatigue strength in nanocrystalline 316 L steel through recovery annealing. Scr. Mater. 217, 114773 https://doi.org/10.1016/j.scriptamat.2022.114773.

Ribárik, G., Gubicza, J., Ungár, T., 2004. Correlation between strength and microstructure of ball-milled Al-Mg alloys determined by X-ray diffraction. Mater. Sci. Eng. A 387–389, 343–347. https://doi.org/10.1016/j.msea.2004.01.089.

Roy, S., Sharma, A., Chaudhari, A., Huang, Y., Langdon, T.G., Suwas, S., 2022. Microstructure evolution and mechanical response of a boron-modified Ti-6Al-4 V alloy during high-pressure torsion processing. Mater. Sci. Eng. A 860, 144124. https://doi.org/10.1016/j.msea.2022.144124.

Sathiyamoorthi, P., Moon, J., Bae, J.W., Asghari-Rad, P., Kim, H.S., 2019. Superior cryogenic tensile properties of ultrafine-grained CoCrNi medium-entropy alloy produced by high-pressure torsion and annealing. Scr. Mater. 163, 152–156. https://doi.org/10.1016/j.scriptamat.2019.01.016.

Schuh, B., Völker, B., Todt, J., Kormout, K.S., Schell, N., Hohenwarter, A., 2018. Influence of annealing on microstructure and mechanical properties of a nanocrystalline CrCoNi medium-entropy alloy. Materials 11 (662), 1–18. https://doi.org/10.3390/ma11050662 (Basel).

Shahmir, H., He, J., Lu, Z., Kawasaki, M., Langdon, T.G., 2016. Effect of annealing on mechanical properties of a nanocrystalline CoCrFeNiMn high-entropy alloy processed by high-pressure torsion. Mater. Sci. Eng. A 676, 294–303. https://doi.org/10.1016/j.msea.2016.08.118.

Shahmir, H., Mehranpour, M.S., Shams, S.A.A., Langdon, T.G., 2023. Twenty years of the CoCrFeNiMn high-entropy alloy: achieving exceptional mechanical properties through microstructure engineering. J. Mater. Res. Technol. 23, 3362–3423. https://doi.org/10.1016/j.jmrt.2023.01.181.

Shah, V., Krugla, M., Offerman, S.E., Sietsma, J., Hanlon, D.N., 2020. Effect of silicon, manganese and heating rate on the ferrite recrystallization kinetics. ISIJ Int. 60, 1312–1323. https://doi.org/10.2355/isijinternational.ISIJINT-2019-475.

Shi, S., Dai, L., Zhao, Y., 2022. Ternary relation among stacking fault energy, grain size and twin nucleation size in nanocrystalline and ultrafine grained CuAl alloys. J. Alloy. Compd. 896, 162953 https://doi.org/10.1016/j.jallcom.2021.162953.

Song, Y., Yoon, E.Y., Lee, D.J., Lee, J.H., Kim, H.S., 2011. Mechanical properties of copper after compression stage of high-pressure torsion. Mater. Sci. Eng. A 528, 4840–4844. https://doi.org/10.1016/j.msea.2011.02.020.

Sonkusare, R., Biswas, K., Al-Hamdany, N., Brokmeier, H.G., Kalsar, R., Schell, N., Gurao, N.P., 2020. A critical evaluation of microstructure-texture-mechanical behaviour heterogeneity in high pressure torsion processed CoCuFeMnNi high entropy alloy. Mater. Sci. Eng. A 782, 139187. https://doi.org/10.1016/j.msea.2020.139187.

Sun, S.J., Tian, Y.Z., Lin, H.R., Yang, H.J., Dong, X.G., Wang, Y.H., Zhang, Z.F., 2018. Transition of twinning behavior in CoCrFeMnNi high entropy alloy with grain refinement. Mater. Sci. Eng. A 712, 603–607. https://doi.org/10.1016/j.msea.2017.12.022.

Tian, X., Zhang, Y., 2009. Effect of Si content on the stacking fault energy in γ-Fe–Mn–Si–C alloys: part I. X-ray diffraction line profile analysis. Mater. Sci. Eng. A 516, 73–77. https://doi.org/10.1016/j.msea.2009.02.031.

Tong, Y., Chen, D., Han, B., Wang, J., Feng, R., Yang, T., Zhao, C., Zhao, Y.L., Guo, W., Shimizu, Y., Liu, C.T., Liaw, P.K., Inoue, K., Nagai, Y., Hu, A., Kai, J.J., 2019. Outstanding tensile properties of a precipitation-strengthened FeCoNiCrTi$_{0.2}$ high-entropy alloy at room and cryogenic temperatures. Acta Mater. 165, 228–240. https://doi.org/10.1016/j.actamat.2018.11.049.

Varvenne, C., Luque, A., Curtin, W.A., 2016. Theory of strengthening in fcc high entropy alloys. Acta Mater. 118, 164–176. https://doi.org/10.1016/j.actamat.2016.07.040.

Wang, Y., Liu, B., Yan, K., Wang, M., Kabra, S., Chiu, Y.L., Dye, D., Lee, P.D., Liu, Y., Cai, B., 2018. Probing deformation mechanisms of a FeCoCrNi high-entropy alloy at 293 and 77 K using *in situ* neutron diffraction. Acta Mater. 154, 79–89. https://doi.org/10.1016/j.actamat.2018.05.013.

Williams, D.B., Carter, C.B., 2009. Transmission Electron Microscopy: A Textbook for Materials Science, 2nd. Springer, Boston, MA.

Williamson, G.K., Hall, W.H., 1953. X-ray line broadening from filed aluminium and wolfram. Acta Metall. 1, 22–31. https://doi.org/10.1016/0001-6160(53)90006-6.

Wu, W., Song, M., Ni, S., Wang, J., Liu, Y., Liu, B., Liao, X., 2017. Dual mechanisms of grain refinement in a FeCoCrNi high-entropy alloy processed by high-pressure torsion. Sci. Rep. 7, 46720. http://doi.org/10.1038/srep46720.

Xie, Z., Xie, J., Hong, Y., Wu, X., 2010. Influence of processing temperature on microstructure and microhardness of copper subjected to high-pressure torsion. Sci. China Technol. Sci. 53, 1534–1539. https://doi.org/10.1007/s11431-010-3157-7.

Yamanaka, S., Ikeda, K., Miura, S., 2021. The effect of titanium and silicon addition on phase equilibrium and mechanical properties of CoCrFeMnNi-based high entropy alloy. J. Mater. Res. 36, 2056–2070. https://doi.org/10.1557/s43578-021-00251-0.

Yeh, J.W., Chen, S.K., Lin, S.J., Gan, J.Y., Chin, T.S., Shun, T.T., Tsau, C.H., Chang, S.Y., 2004. Nanostructured high-entropy alloys with multiple principal elements: novel alloy design concepts and outcomes. Adv. Eng. Mater. 6, 299–303. https://doi.org/10.1002/adem.200300567.

Yoshida, S., Bhattacharjee, T., Bai, Y., Tsuji, Y., 2017. Friction stress and Hall-Petch relationship in CoCrNi equi-atomic medium entropy alloy processed by severe plastic deformation and subsequent annealing. Scr. Mater. 134, 33–36. https://doi.org/10.1016/j.scriptamat.2017.02.042.

Zhang, J.Y., He, Q.F., Li, J., Yang, Y., 2021. Chemical fluctuations enabling strength-plasticity synergy in metastable single-phase high entropy alloy film with gigapascal yield strength. Int. J. Plast. 139, 102951. http://doi.org/10.1016/j.ijplas.2021.102951.

Zhang, T.W., Ma, S.G., Zhao, D., Wu, Y.C., Zhang, Y., Wang, Z.H., Qiao, J.W., 2020. Simultaneous enhancement of strength and ductility in a NiCoCrFe high-entropy alloy upon dynamic tension: micromechanism and constitutive modeling. Int. J. Plast. 124, 226–246. https://doi.org/10.1016/j.ijplas.2019.08.013.

Zhang, Y., Zhou, Y.J., Lin, J.P., Chen, G.L., Liaw, P.K., 2008. Solid-solution phase formation rules for multi-component alloys. Adv. Eng. Mater. 10, 534–538. https://doi.org/10.1002/adem.200700240.

Zhao, W., Han, J.K., Kuzminova, Y.O., Evlashin, S.A., Zhilyaev, A.P., Pesin, A.M., Jang, J., Liss, K.D., Kawasaki, M., 2021. Significance of grain refinement on micro-mechanical properties and structures of additively-manufactured CoCrFeNi high-entropy alloy. Mater. Sci. Eng. A 807, 140898. https://doi.org/10.1016/j.msea.2021.140898.

Zhilyaev, A.P., Nurislamova, G.V., Kim, B.K., Baro, M.D., Szpunar, J.A., Langdon, T.G., 2003. Experimental parameters influencing grain refinement and microstructural evolution during high-pressure torsion. Acta Mater. 51, 753–765. https://doi.org/10.1016/S1359-6454(02)00466-4.

Zhu, Y.T., Liao, X.Z., Wu, X.L., 2012. Deformation twinning in nanocrystalline materials. Prog. Mater. Sci. 57, 1–62. https://doi.org/10.1016/j.pmatsci.2011.05.001.